AIAA AVIATION Forum
5-9 June 2017, Denver, Colorado
47th AIAA Fluid Dynamics Conference

Measurements in the Boeing/AFOSR Mach-6 Quiet Tunnel on Hypersonic Boundary-Layer Transition

Brandon C. Chynoweth*, Joshua B. Edelman*, Kathryn A. Gray*, Gregory R. McKiernan*, and Steven P. Schneider†
School of Aeronautics and Astronautics
Purdue University
West Lafayette, IN 47907-1282

This paper presents results from four different research projects currently ongoing at Purdue University. (1) Different criteria for detecting the edge of the boundary layer were investigated on the flared cone geometry. It was determined that a method based on the total enthalpy profile would be used for future edge-detection computations on the flared cone geometry. A Rod Insertion Method (RIM) roughness insert was measured using a Zygo ZeGage optical profiler. Experimental results with a single RIM insert are presented. Maximum second-mode magnitudes of nearly 27% were measured 2.5 cm upstream from where spectral filling and intermittency algorithms compute that transition has begun. (2) Preliminary data from a new model shows that high-frequency secondary instabilities of stationary crossflow waves are localized under the troughs of the stationary vortices. Measurements of the growth of the secondary instabilities are reported for two different vortices. (3) In order to better understand the effects that probe geometry has on measured pressure fluctuations, pitot measurements were taken using various sleeves which alter the forward-facing diameter of the probe. The results indicate a clear effect of probe size on the measured power spectral densities. Furthermore, it was found that the geometry effects are Reynolds number dependent. (4) Experiments on a cone with a slice and ramp were completed to determine if transitional shock wave-boundary layers interactions can be measured within the Boeing/AFOSR Mach-6 Quiet Tunnel. Initial experiments showed that with a newly designed model it is possible to measure transitional interactions.

Nomenclature

δ	boundary-layer thickness
χ	transfer function
f	frequency
M	Mach number
p	pressure
θ	azimuthal angle
Re_x	Reynolds number based on sensor axial distance
Re_∞	unit Reynolds number
T	temperature
x	model axial coordinate
y	distance from tunnel centerline
z	distance from tunnel throat

Subscripts

0	stagnation condition
∞	freestream condition
min	minimum value
peak	peak value
wall	wall condition

Abbreviations

AEDC	Arnold Engineering Development Center
BAM6QT	Boeing/AFOSR Mach-6 Quiet Tunnel
IR	Infrared
NUDT	National University of Defense Technology
PEEK	Polyether ether ketone
PSD	Power-Spectral Density
RIM	Rod Insertion Method
RMS	Root-Mean Squared
SBLI	Shock Boundary Layer Interaction
STABL	Stability and Transition Analysis for Hypersonic Boundary Layers
TSP	Temperature-Sensitive Paint

*Research Assistant. Student Member, AIAA
†Professor. Associate Fellow, AIAA

I. Introduction

A. Hypersonic Boundary-Layer Transition

Boundary-layer transition affects the heating, skin friction, drag, and moments that a vehicle may experience in flight. A transitional or turbulent boundary layer may have heating rates that are three or more times larger than during laminar conditions. Early boundary-layer transition can cause a heat shield to ablate faster than anticipated and lead to vehicle failure. If a designer takes the worst-case scenario approach, the heat shield may be excessively heavy, reducing the maneuverability and range of the vehicle. Boundary-layer transition may not occur symmetrically, and the vehicle can experience asymmetric loads. If the control system is not robust enough, the vehicle may be lost.[1] Factors such as Mach number, the freestream disturbance environment, nose bluntness, and wall temperature can all have significant impacts on the location of the transition region.[2] How these factors interact with physical mechanisms is still not well understood, and therefore empirical or semi-empirical prediction methods are currently used when designing vehicles. The goal of experiments performed in the Boeing/AFOSR Mach-6 Quiet Tunnel is to better understand the physical mechanisms of instabilities at hypersonic speeds and to aid in the development of mechanism-based transition prediction methods.

B. The Boeing/AFOSR Mach-6 Quiet Tunnel

The Boeing/AFOSR Mach-6 Quiet Tunnel (BAM6QT) has the highest quiet Reynolds number of any of the hypersonic quiet tunnels presently known to be operational anywhere in the world. It has been quiet to a unit Reynolds number of over 12.5×10^6/m,[3] which is higher than the well-known tunnel at Texas A&M (the former NASA Langley tunnel).[4] The importance of quiet wind tunnels for hypersonic boundary-layer transition experiments as outlined by Schneider[5] has led to the development of new facilities. Performance of the Peking University quiet tunnel is not well documented in the open literature, but that tunnel is smaller and seems to be quiet only at lower unit Reynolds numbers.[6,7] The new National University of Defense Technology (NUDT) tunnel in Changsha, Hunan, China is larger (300 mm diameter nozzle), but the recent AIAA paper announcing the first measurements in this tunnel contains almost no information about the performance of the facility, which seems to be quiet only below a stagnation pressure of about 70 psia.[8]

The BAM6QT is a Ludweig tube design incorporating a long driver tube with a converging-diverging nozzle at the downstream end. A schematic of the facility is shown in Figure 1. Operation of the tunnel begins when a pair of diaphragms, which separate the high pressure driver tube from the vacuum tank, are burst causing an expansion fan to propagate upstream. Once the expansion fan has passed through the throat, the air behind the expansion fan is accelerated through the nozzle initiating Mach 6 flow. Approximately every 200 ms, the expansion fan reflects from the contraction causing the stagnation pressure to drop. During each 200 ms period between reflections, the conditions of the flow are quasi-static. With a run time of approximately 5 seconds, collecting data at a range of Reynolds numbers is possible during a single run.

The BAM6QT incorporates several unique features to maintain a laminar boundary layer on the nozzle wall, promoting a low-noise environment comparable to flight conditions. The long divergent portion of the nozzle was designed to minimize the Görtler instability. Additionally, it is polished to a mirror finish to reduce any roughness that may lead to transition of the nozzle wall boundary layer. A series of filters eliminates particles larger than 0.01μm from the air used to pressurize the driver tube, to help protect the mirror finish of the nozzle. Just upstream of the throat, a suction slot connected to the vacuum tank can be used to remove the contraction wall boundary layer. This forces a fresh laminar boundary layer to grow on the nozzle wall starting at the bleed lip. Using the suction slot, the BAM6QT produces freestream pitot pressure fluctuations less than 0.02% of the mean.[9] If a noise level similar to conventional hypersonic facilities is desired, the operator can close the bleed valve, creating pressure fluctuations that are approximately 3% of the mean pressure.

Since December of 2016, the facility has been operating at a reduced maximum quiet pressure of 135 psia after replacement of an o-ring in the contraction. Work is ongoing to eliminate dust particles that may be leading to this reduction in performance.

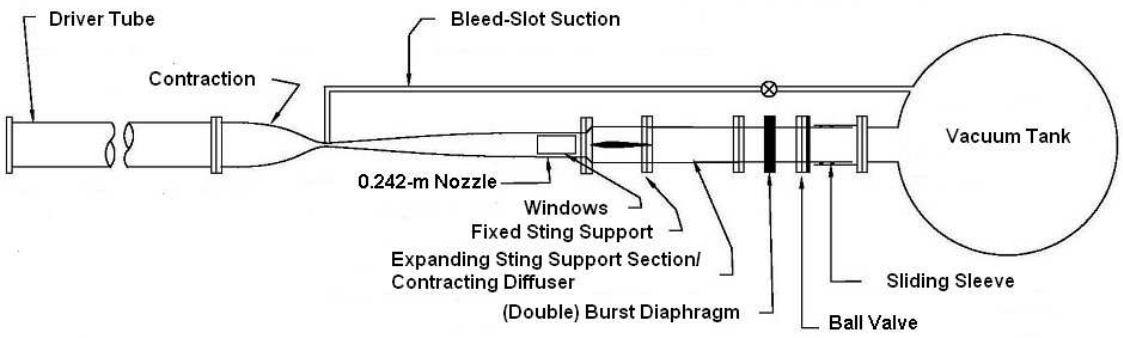

Figure 1. Schematic of Boeing/AFOSR Mach 6 Quiet Tunnel (BAM6QT) located at Purdue University.

II. Computational Work on the Flared Cone Geometry

A. Boundary-Layer Edge Determination

The boundary-layer edge plays an important role in hypersonic stability research. The boundary layer thickness, δ, can be used to estimate the second-mode instability frequency, and current research by Marineau[10] seeks to determine if a relationship between the maximum second-mode wave magnitude and the edge Mach number can be used to help develop a new method to predict hypersonic laminar-turbulent transition. Historically, the determination of the boundary-layer thickness is not trivial. For subsonic speeds, often times it is simply identified as the point where the velocity reaches a certain percentage of the freestream velocity. At supersonic and hypersonic speeds, this simple definition begins to break down as oblique shocks, heat transfer, and other flow properties start to have significant effects. Since hypersonic flows can involve both high speeds and temperatures, a boundary-layer edge criteria based on the total enthalpy, H, may be appropriate to use.

A brief overview of previous boundary-layer edge detection work at hypersonic speeds is now presented to show that no universal criteria exists for edge detection. In fact, most likely there is no "correct" answer for determining δ for a geometry, but with careful consideration of different flow parameters the edge may be inferred in a logical manner. Bertin notes the inviscid region outside the boundary layer of a hypersonic flow is assumed to be adiabatic so that the gradient of the total enthalpy in the wall-normal direction goes to zero moving outward from surface.[11] A caveat is that if a flow contains an enthalpy overshoot, the gradient is zero both near the boundary-layer edge as well as at the point where the maximum overshoot occurs as shown in Figure 2. A short review of literature shows that the there is no universal way to determine the boundary-layer edge. Using the Stability and Transition Analysis for Hypersonic Boundary Layers (STABL) software package developed by the University of Minnesota, Jewell[12] performed mean flow and stability computations of the classic Stetson experiments[13] on a cone with various nosetip bluntnesses at Mach 6. The point of maximum enthalpy overshoot was used to define the boundary-layer edge to determine the edge Mach number and unit Reynolds number. Adams, Jr. et. al[14] performed boundary-layer computations to compare with tests conducted at Arnold Engineering Development Center (AEDC) Tunnel B on the centerline of the Space Shuttle Orbiter at 30° angle of attack. Since the Shuttle Orbiter had a complex three dimensional shape, computations were performed on an axisymmetric hyperboloid geometry that resulted in similar bow shock and surface pressure distributions as experimental results on the centerline of the test article. Adams, Jr. et. al used a boundary-layer edge criteria based on previous work by Levine.[15] Their methodology starts near the shock and marches towards the surface until the ratio of the local total enthalpy to the freestream total enthalpy, H/H_∞, differs by 0.005 from unity. They note that for enthalpy profiles with an overshoot this results in the boundary-layer edge at a location where $H/H_\infty = 1.005$, and for enthalpy profiles without an overshoot δ is at a point where $H/H_\infty = 0.995$. The computed boundary-layer thickness,

edge Mach, and edge Reynolds number for the paraboloid were compared to experimental results on the centerline of the Space Shuttle Orbiter. Figure 5 in their Journal of Spacecraft and Rockets paper shows good agreement between computations and experiments when using this method to determine the edge conditions. The boundary layer thickness is sensitive not only to the criteria used to determine the edge, but also to the type of computational approach. In Berry et. al[16] three different computational methods were used to compute the boundary-layer edge properties on the windward side of the Space Shuttle Orbiter. Comparing different computational approaches, edge Mach numbers differed by up to 20% and δ differed by nearly 50%.

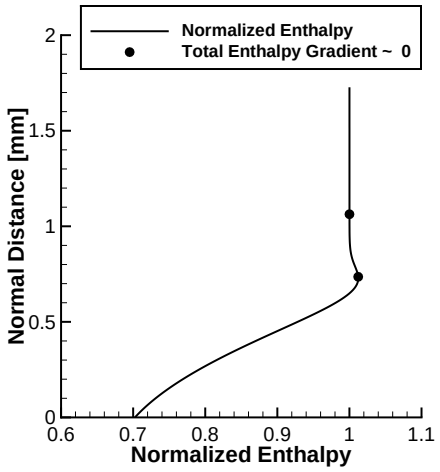

Figure 2. Near wall total enthalpy profile on the flared cone geometry at x = 9.742 cm showing the total enthalpy overshoot and points where the gradient of the total enthalpy approaches zero. Enthalpy is normalized by freestream total enthalpy, H_∞.

B. STABL Edge Detection Algorithms

Currently STABL has four different built-in methods to determine the boundary-layer edge using the total enthalpy profile, but only three were used for the current study. The methods that were investigated were the "Total enthalpy first reached", the "Peak total enthalpy overshoot", and the "Return from enthalpy overshoot." For each method the user must input an "Edge detection rbl" value between 0 and 1, the meaning of which varies based on the edge detection method used. The value will be denoted by RBL from this point forward.

The "Total enthalpy first reached" method begins at the wall surface and moves outward until the enthalpy, H, reaches

$$H > RBL \times H_\infty + H_{wall} \times (1 - RBL) \tag{1}$$

where the subscript "wall" indicates the total enthalpy at the wall and "∞" indicates the total enthalpy in the freestream. The boundary-layer edge is the first point where Equation 1 is satisfied.

For enthalpy profiles that have an overshoot above the freestream value, two different methods are available. The first method is the "Peak total enthalpy overshoot." In order to properly detect the peak overshoot, an RBL = 1.0 must be used. If other values are used, the peak will not be properly detected. A second method determines when the total enthalpy returns to near freestream values after the overshoot has occured, and was first suggested by Tyler Robarge.[17] The "Return from enthalpy overshoot" method first determines the point where the peak overshoot occurs. Once the peak is detected, the algorithm moves away from the wall until the enthalpy has returned to a value near the freestream values. The total enthalpy at the boundary-layer edge satisfies

$$H < \frac{|H_\infty - H_{wall}|}{RBL} + H_{wall} \tag{2}$$

C. Results on the Flared Cone Geometry

Transition at Mach 6 on axisymmetric geometries near zero degrees angle of attack is dominated by the second-mode instability. The second-mode wave is similar to a trapped acoustic wave that reflects between the surface of a model and the sonic line within the boundary layer.[18] The nature of this reflection results in the tuning of the second-mode instability to the boundary-layer thickness. A flared cone model was designed by Wheaton[19] to maintain a boundary layer with a near constant thickness which amplifies a narrow band of second-mode instability frequencies. The flared cone geometry has a 3-meter circular arc with a sharp nosetip. In order to compare maximum second-mode magnitudes in a quiet flow facility to the work of Marineau,[10] it is necessary to compute the Mach number at the edge of the boundary layer.

Figures 3 and 4 show the Mach number, velocity, and total enthalpy profiles near the surface of the cone at an axial distance of 9.742 cm and 26.438 cm from the nosetip, respectively. The very first edge-detection method tested on the flared cone geometry was a simple velocity criterion. The edge was determined as the point where the velocity reached 99% of the post-shock velocity. Figure 3 shows that this δ is approximately 0.8 mm at a distance of 9.742 cm from the nosetip. Further downstream at x = 26.438 cm the δ is 3.1 mm from the wall and it is not shown in Figure 4. The total enthalpy gradient is zero after approximately 1.5 mm, so it seems likely that this criteria does not provide a reliable estimate of the boundary-layer edge.

Four other criteria using STABL were tested on the flared cone geometry based on personal communications with Dr. Bradley Wheaton[20] and Dr. Eric Marineau[21] and are summarized in Table 1. The cases were tested on a STABL simulation of the flared cone model at a stagnation pressure of 160 psia, a stagnation temperature of 425 K, and a model wall temperature of 300 K. While it is not possible to pick the "correct" method, one can judge the quality of the boundary-layer edge detection based on several factors. Inside the boundary layer, large gradients may exist in the velocity, Mach number, and other quantities, but outside the boundary layer significant gradients should not occur.

Table 1. Summary of edge detection methods implemented in STABL on a flared cone simulation.

	Method	RBL Value
Case 1	Total enthalpy first reached	0.995
Case 2	Total enthalpy first reached	0.999
Case 3	Peak total enthalpy overshoot	1.000
Case 4	Return from enthalpy overshoot	0.997

The first case tested was determined using the "Total enthalpy first reached" method with RBL = 0.995. It can be seen in Figures 3 and 4 that Case 1 occurs below the enthalpy overshoot and a significant velocity gradient exists outside the boundary layer. Figure 5 shows that the edge Mach number is well below 4.0 over the entire length of the model and a significant oscillation in the calculated edge Mach number occurs. These oscillations are due to the spacing between grid points and the large Mach number gradients present within the boundary layer. Increasing the RBL parameter to 0.999, Case 2, does not have a significant effect on either the boundary-layer thickness or the edge Mach number distribution.

Since the enthalpy profiles exhibit an overshoot, the two methods that incorporate the overshoot into the edge-detection algorithm were tested. Case 3 determined the boundary-layer edge by using the "Peak total enthalpy overshoot" method. It can be seen in Figure 4 that this infers a thicker boundary layer, but the calculated edge Mach number in Figure 5 still has an oscillatory nature for almost the entire length of the model. In Figure 3, the Mach number doubles from 2.8 to 5.7 over a distance covered by 31 grid points. Increasing the number of wall-normal grid points in the region of large Mach gradients may eliminate the oscillations observed in Figure 5 at the cost of increased computational time.

Finally the "Return from enthalpy overshoot" (Case 4) method was used. Several different RBL values were tested, but only the results for one are presented. With RBL = 0.997, the boundary-layer edge is just under 0.9 mm and 1.2 mm from the surface for the two different locations on the model. At this point, no large gradients in the velocity, edge Mach number, or total enthalpy exist outside the boundary layer. The edge Mach number profile in Figure 5 shows a steadily decreasing Mach number without any oscillations over

the entire length of the model. Based on this observation, the "Return from enthalpy overshoot" with and RBL = 0.997 was used for the boundary-layer edge detection method for all STABL computations performed on the flared cone geometry. It should be noted that for the four cases tested, the edge Mach number varied by almost a factor of two. This sensitivity to the boundary-layer edge detection method should be kept in mind for future geometries as a different edge detection method may be necessary.

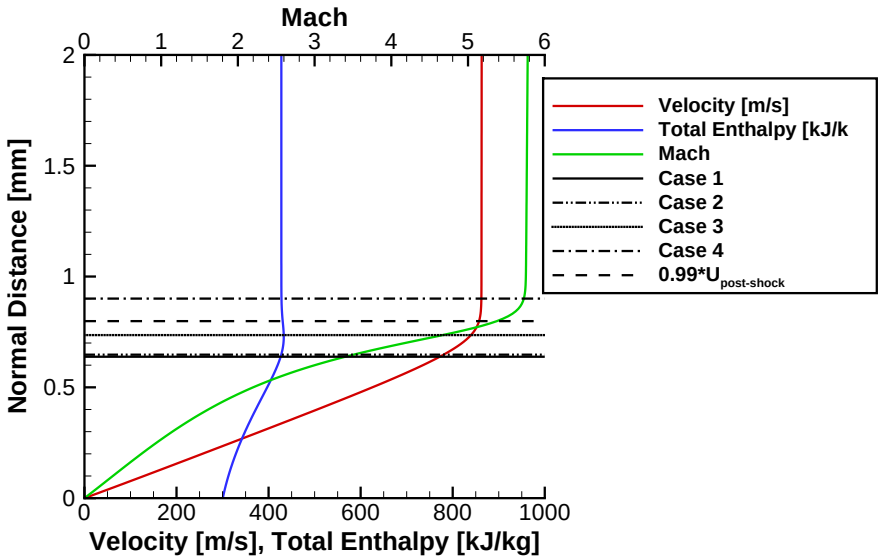

Figure 3. Mach number, velocity, and total enthalpy profiles near the flared cone surface at x = 9.742 cm from the nosetip. Horizontal lines denote boundary-layer edge using different detection methods.

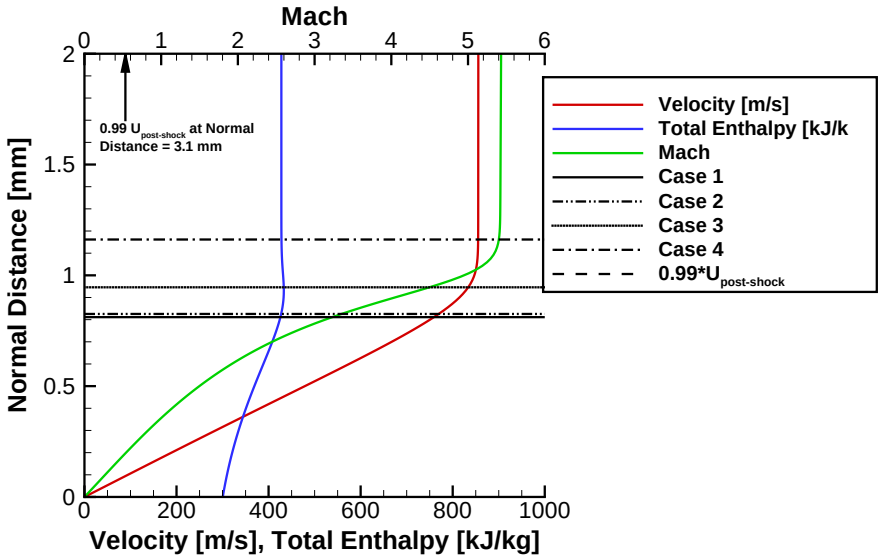

Figure 4. Mach number, velocity, and total enthalpy profiles near the flared cone surface at x = 26.438 cm from the nosetip. Horizontal lines denote boundary-layer edge using different detection methods.

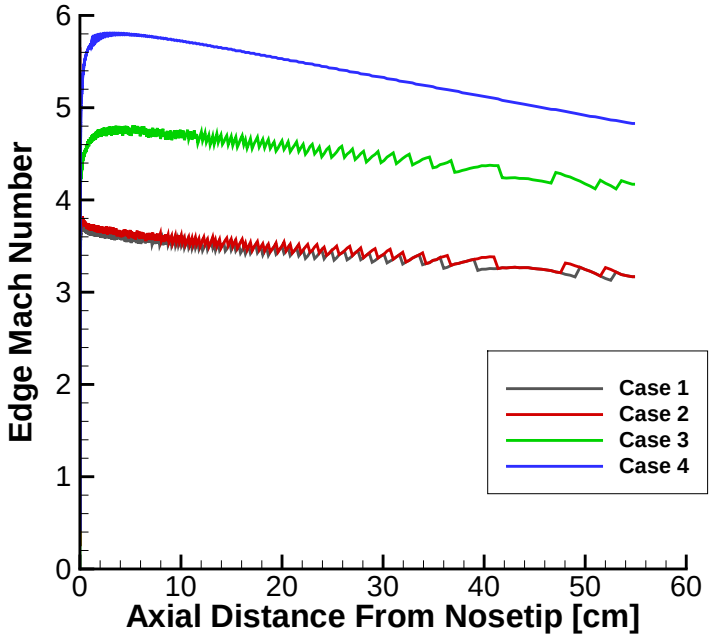

Figure 5. Mach number distribution over the entire length of the flared cone for the four different cases.

III. New Experimental Results on the Flared Cone Geometry

Experiments were performed using the 4.5-inch base diameter flared cone. The main sensor ray now has 13 PCB132A31 fast-pressure sensors for high fidelity measurements of the growth, saturation, and breakdown of the second-mode instability. Four PCB sensors spaced 90° apart azimuthally were used to align the model to 0.0° angle of attack. The model was painted with temperature sensitive paint (TSP) for global visualization of the heat flux to the model surface. The current goal is to relate the growth and breakdown of the second-mode waves to the heating patterns observed on the model surface. In addition, the peak second-mode wave magnitude and its relationship to the onset of transition is also being studied.

A. Results Using a Rod Insertion Method (RIM) Insert for Controlled Roughness

The Rod Insertion Method (RIM) insert was developed for the creation of well-controlled roughness elements that could be inexpensively and quickly manufactured at Purdue University. Measurements of the roughness elements on a RIM insert were performed using a Zygo ZeGage optical profiler and a precision sample rotation apparatus. The insert was designed to have roughness elements with a diameter of 0.033", a height of 0.010", and a center-to-center spacing of 12°. Figure 6 is an azimuthal profile of the roughness elements across the field of view that is normally processed in the TSP images. The roughness element centered at 0° is placed directly upstream of the main sensor ray when performing experiments. Measurements show that the individual elements are all nearly 0.009" in height. Although the as built roughness are not as accurate as hoped, these small variations still seem acceptable. Now that the roughness element heights have been measured, trends and patterns based on actual roughness heights can be formulated more accurately.

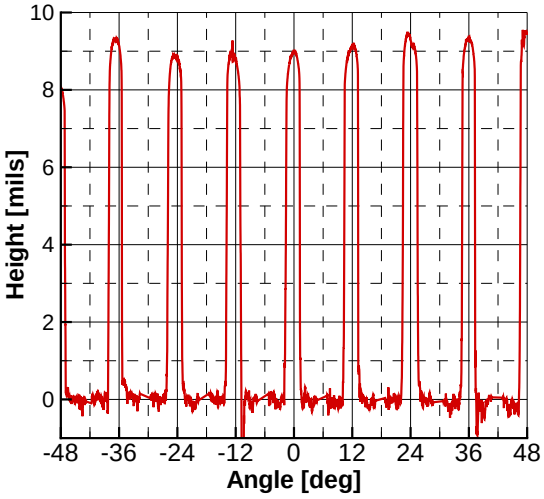

Figure 6. Profile of RIM roughness insert centered around roughness element placed directly upstream of main sensor ray during experiments.

An initial Mach-6 tunnel experiment was performed with a roughness element directly upstream of the main sensor array. The magnitude of the second-mode wave was calculated at the exposure time of each TSP image by computing the power spectral density (PSD) and then integrating from 200 to 400 kHz. This bandwidth was chosen because the second-mode wave was experimentally observed to be centered at approximately 300 kHz. A method developed by Casper[22] was used to compute the intermittency at the same time as each PSD. A certain degree of uncertainty exists in the intermittency calculation since the algorithm depends on arbitrary thresholds that the user must tune to each data set. Figure 7(a) shows the PSD of each sensor computed at the time when the peak magnitude was measured. Figure 8 has the magnitude of the second-mode peak and the intermittency for the same data. Figure 9 is a TSP image processed at the corresponding time with flow from right to left. The red line is just upstream of the sensor that measures the maximum second-mode magnitude. Comparison of the pressure and TSP data at the time of the peak magnitude provides many interesting insights into the growth and breakdown of the second-mode wave:

1. The peak pressure fluctuation magnitude is measured by the sensor at 44.1 cm when the intermittency is still approximately zero. The peak second-mode magnitude of 26.8% was measured at a freestream unit Reynolds number of 9.21×10^6/m($P_0 = 115.9$ psia, $T_0 = 414$ K). The TSP image shows this sensor is in the middle of the first increase in streak heating.

2. Figure 10 is an azimuthal profile taken at the location of the red line in Figure 9 overlaid with the Zygo measurements of the roughness elements. It shows that directly downstream from each roughness element a single hot streak develops beginning at approximately 43 cm.

3. A pair of streaks begins to develop downstream of the gap between roughness elements starting near 40 cm from the nosetip. The PSD of the sensor at 40.3 cm shows the first indications of the second-mode bandwidth broadening.

4. The first significant increase in intermittency is computed at the sensor 46.6 cm from the nosetip, located in the cooler region downstream of the first increase in heating. This is 2.5 cm downstream of where the peak fluctuation was measured.

5. The intermittency at the furthest downstream sensor is just below 0.5. This sensor is just at the beginning of the downstream region of increased heating, and the pressure fluctuations have dropped to less than 5%. Transition to fully turbulent flow was not measured.

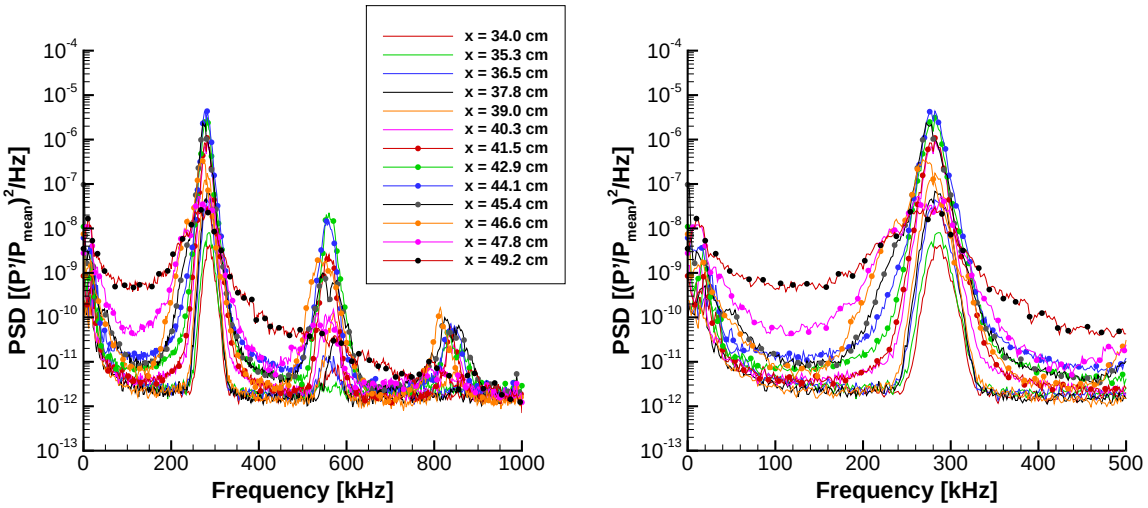

(a) PSD

(b) Enlarged PSD

Figure 7. PSD processed at the time of the maximum second-mode wave magnitude ($Re = 9.21\times10^6$/m, P_0 = 115.9 psia, T_0 = 414 K) measured by the PCB at x = 44.1 cm. Enlarged view shows second-mode bandwidth starting to broaden at x = 40.3 cm.

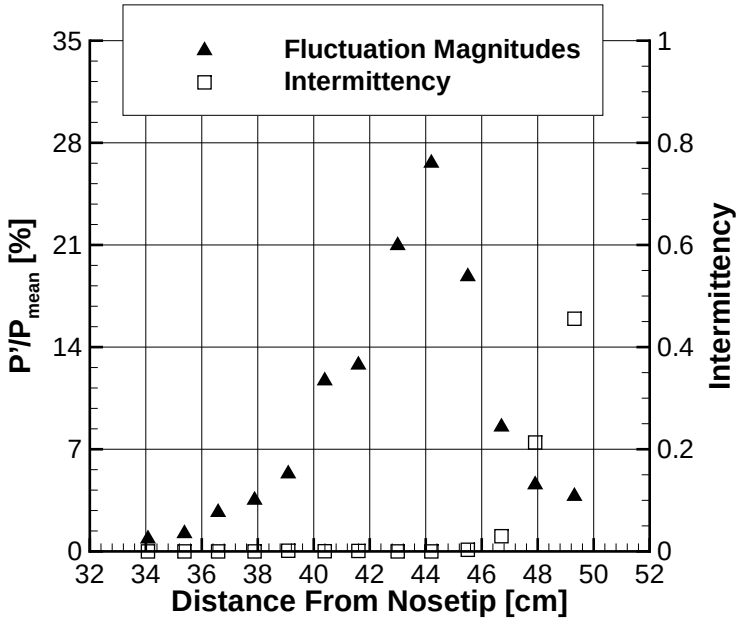

Figure 8. Second-mode magnitudes and computed intermittency processed at the time of the maximum second-mode wave magnitude. ($Re = 9.21\times10^6$/m, P_0 = 115.9 psia, T_0 = 414 K)

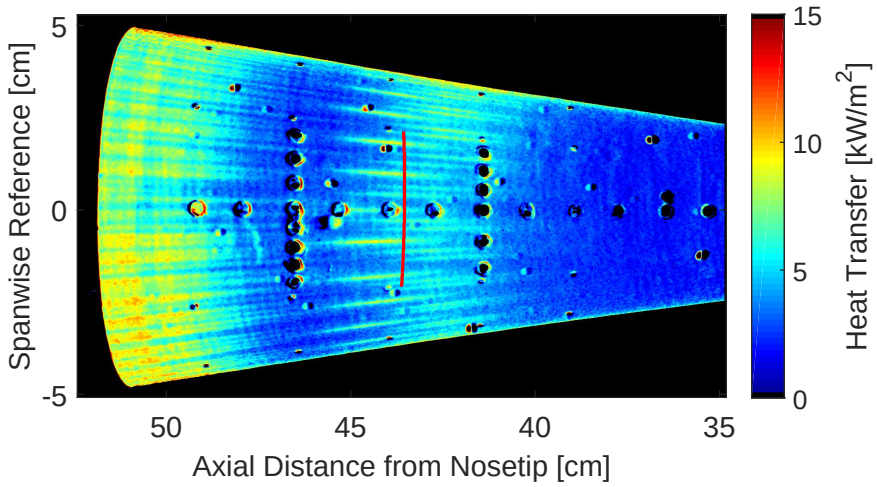

Figure 9. TSP image of flared cone taken at the time of the maximum second-mode wave amplitude. The red line is the location of the azimuthal heat transfer profile in Figure 9. ($Re = 9.21\times10^6$/m, P_0 = 115.9 psia, T_0 = 414 K)

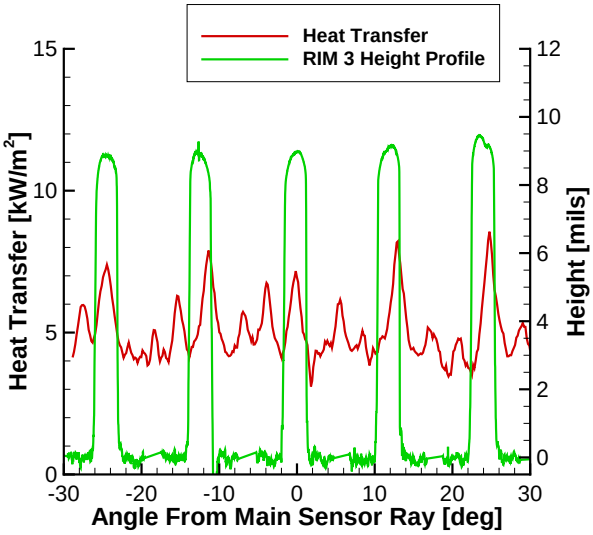

Figure 10. Azimuthal heat transfer profile for a 60° field of view centered on the main sensor ray. Roughness profile overlaid to show relationship between heating and roughness element placement.

Testing is ongoing with RIM inserts of varying roughness element heights, diameters, and spacings. Results will be compared to analyze the effect of the RIM roughness on the maximum second-mode magnitude, the observed heating pattern, and other characteristics. Additionally, a new model flared cone model is being fabricated to obtain better measurements of the growth and breakdown of the second-mode instability. With an expected graduation date of December 2017, the author is focusing on obtaining data sets that have high quality PCB and TSP data. Additionally, a slender straight cone with a half-angle of 2.5° may be tested to study transition due to the second-mode instability without the added effects of surface curvature.

IV. Effects of Probe Size on Pressure Fluctuation Measurements

Characterization of the noise levels in a wind tunnel is crucial, and many methods have been developed for this task. In the BAM6QT, the most common apparatus used is a pitot probe containing a pressure transducer. However, a bow shock is formed in front of the sensor, through which the flow must pass before being measured. It is therefore impossible to directly measure the freestream disturbances. The relationship between the pre- and post-shock pressure fluctuations is described by the transfer function, defined in this case by the ratio of measured to freestream power spectral densities. Because the freestream cannot be directly measured, the transfer function cannot be determined experimentally but can be estimated numerically. The measurements presented here examine the effects of probe size on the measured fluctuations. This data will later be compared to work done by Chaudhry and Candler,[23] who have computed the transfer functions using direct numerical simulation and shown that an acoustic disturbance reflects between the shock and pitot-probe face. Simulations are being performed using a variety of freestream disturbance sources and incidence angles. These will be compared to the experimental results.[24]

A. Instrumentation

This work follows that done by Sweeney.[25] The goal for this experiment was to compare the pressure fluctuations measured by a pitot probe with four different forward-facing diameters. The control geometry used for these measurements consists of a B-Screen Kulite model XCQ-062-015 pressure transducer protruding from a brass sleeve in a probe support (Figure 11(a)). The forward-facing diameter of the probe was changed using the three sleeves shown in Figure 11(b). Note that the brass sleeve used in the no-sleeve case is much smaller than the three sleeves used to adjust the forward-facing diameters, which cover the brass sleeve completely and fit over the stainless steel rod. The two larger sleeves were designed by Sweeney[25] and the smallest was a modification of his design. Each sleeve consists of a 0.04 in long cylindrical section, a circular cone section with some half-angle, and a cylindrical support section 0.22 in long which contains four set screws used to secure the sleeve on the probe support. Table 2 lists the dimensions of each sleeve. The sleeve length is the total sleeve length, including the two cylindrical sections and the cone section. For the no-sleeve case, the base diameter refers to the diameter of the probe support, which is the stainless steel rod shown on the right of Figure 11(a). The same Kulite sensor was used for each case, and although the half-angle of the sleeves varies, the most significant difference is assumed to be the forward-facing diameter.

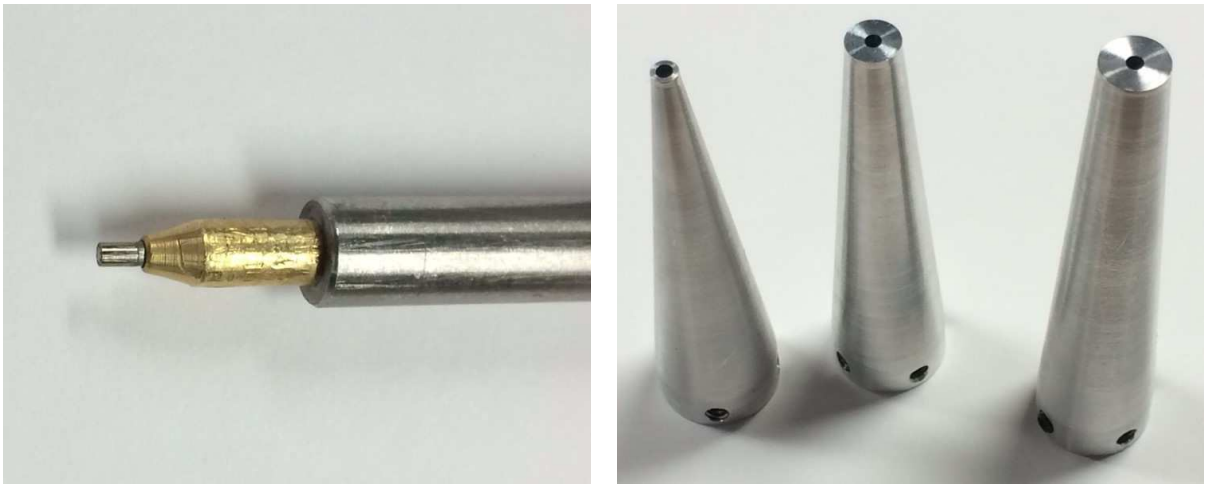

(a) The probe for the "no sleeve" case.

(b) The sleeves used to modify the forward-facing diameter.

Figure 11. Photographs of the probe geometries used for current experiments.

Table 2. Dimensions of probe geometries with and without sleeves.

Geometry	Forward-Facing Diameter	Base Diameter	Sleeve Length	Sleeve Half-Angle
No Sleeve	0.066 in	0.315 in	-	-
Small Sleeve	0.118 in	0.6 in	2.25 in	6.905°
Medium Sleeve	0.236 in	0.564 in	2.25 in	4.711°
Large Sleeve	0.283 in	0.564 in	2.5 in	3.576°

B. Results

All measurements presented here were taken on the Mach-6 tunnel centerline at an axial location of $z = 92$ in downstream from the throat. Additional off-centerline measurements were taken at a height of $y = 1$ in above the centerline to ensure no centerline effects were influencing the data, but are not presented here because they showed identical results to the centerline measurements. Initial stagnation pressures of both $P_0 = 130$ psia and $P_0 = 45$ psia were used to determine any Reynolds number effects. All data presented here were taken under noisy flow conditions with the bleed valves closed.

The power spectral densities of the normalized pressure fluctuations were calculated from segments of data 0.1 seconds in length that occurred approximately 1 second into the run. The precise time of the data segment was determined by the stagnation pressure to ensure a specific Reynolds number for each run. In all cases, the pressure fluctuations are normalized by the mean pitot pressure during the 0.1 second segment of data. Figure 12 shows the power spectral densities for each sleeve at two different Reynolds numbers. It should be noted that although data from only one run are shown for each case, this is simply to prevent a cluttered plot. Multiple runs were taken for each set of conditions, and only data that have been verified by similar results are presented here. The peak around $f = 260$ kHz indicates the resonance of the Kulite and is not a feature of the flow. For both Reynolds numbers, similar trends can be seen with respect to the forward-facing diameter. The no-sleeve case resulted in noticeably larger pressure fluctuations for most of the frequency range compared to the three cases where a pitot sleeve was used. At lower frequencies ($f \leq 50$ kHz) the PSD for the large sleeve and the medium sleeve are very similar. Finally, an increase can be seen around $f = 150$ kHz for all cases. It is possible that this is due to a resonance between the sensor face and the shock wave produced by the probe.

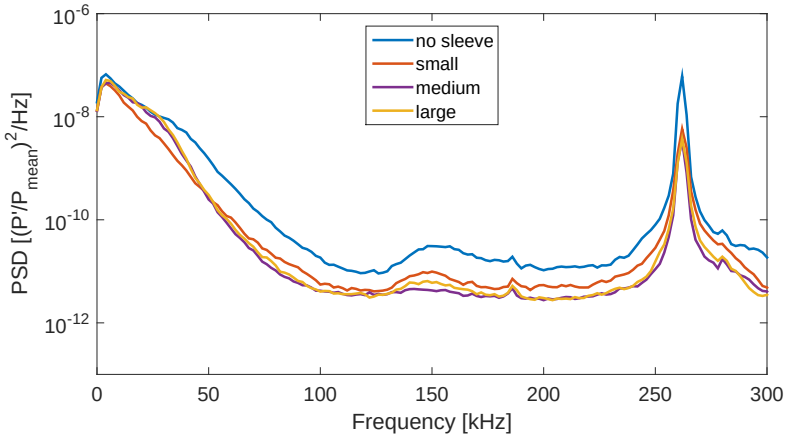

(a) Re = 3.5×10^6/m

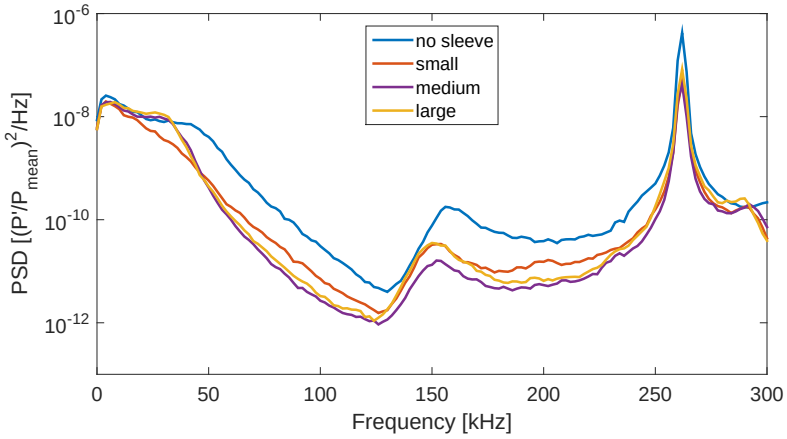

(b) Re = 10.1×10^6/m

Figure 12. PSDs of pressure fluctuations for the four probe geometries for two Reynolds numbers. Probe located on the centerline at $z = 92$ in downstream of the throat.

It is important to reiterate that the above PSDs do not represent the freestream fluctuations, but rather those that have passed through the shock wave produced by the pitot probe. The freestream cannot be directly measured, so it is of interest to determine the transfer function of the probe, which could then be used to determine the freestream fluctuations. Because it is not possible to experimentally measure the transfer function, it must be calculated from simulations. The following simple method of combining the results from multiple probes was suggested by Chaudhry[24] and allows numerical and experimental comparisons. The transfer function χ is defined such that:

$$\chi_{probe} = \frac{PSD_{probe}}{PSD_{\infty}} \tag{3}$$

The ratio of the transfer function of a probe with a sleeve to that of the sensor without a sleeve is then given by:

$$R_{sleeve} = \frac{\chi_{sleeve}}{\chi_{no-sleeve}} = \frac{PSD_{sleeve}}{PSD_{no-sleeve}} \tag{4}$$

Thus, this ratio allows direct comparisons to be made between the experimental measurements of the power

spectral densities and numerical calculations of the transfer function. Although no comparisons to simulations will be made in this paper, the ratio uses the no-sleeve case to normalize the other pitot probe diameters and is therefore useful when examining the effects of probe size on the measured results.

The ratios defined in Equation 4 are computed from the PSDs previously shown for each sleeve and Reynolds number, and are presented in Figure 13. Once again, the results for the large sleeve and the medium sleeve are similar and the small-sleeve case yields noticeably different results. This is especially true for the lowest Reynolds number. An increase in the ratio for all three sleeves at just under $f = 150$ kHz is present at both Reynolds numbers, and the center of the peak is located at a higher frequency for the largest Reynolds number.

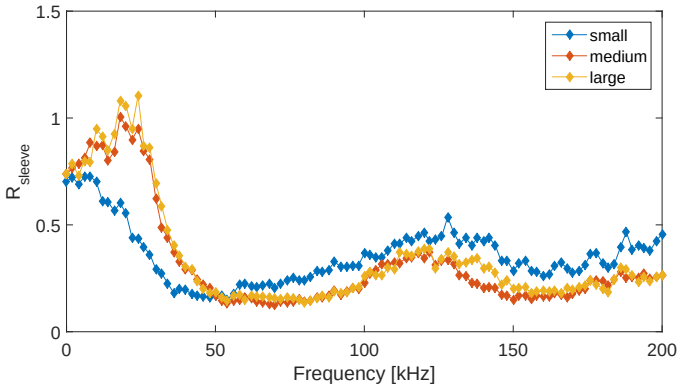

(a) Re = 3.5×10^6/m

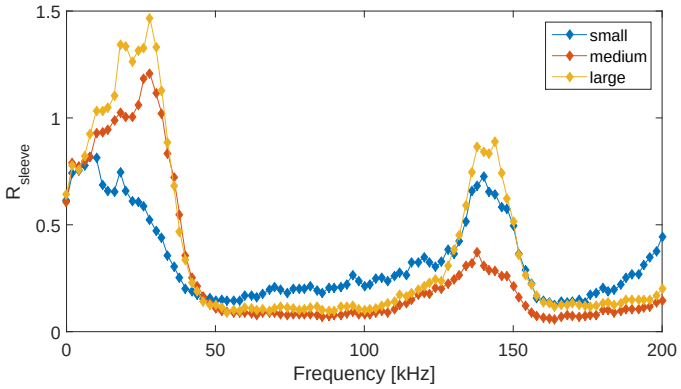

(b) Re = 10.1×10^6/m

Figure 13. The ratios of the PSDs from the probes with the various sleeves to the PSD of the no-sleeve case.

To better determine a possible Reynolds number effect, the ratios for both Reynolds numbers are plotted for a given sleeve size in Figure 14. For each sleeve, the peak in the ratio at frequencies below 50 kHz is larger for the higher Reynolds number. Furthermore, the difference between the two Reynolds numbers increases with increasing sleeve diameter. Additionally, the increase in pressure fluctuations near 150 kHz is larger when the Reynolds number is higher for the small and large sleeves. However, for the medium sleeve, the increase is approximately the same for both Reynolds numbers. The reasons for this peak or for the difference in behavior for the medium sleeve are unknown at this time. However, the Reynolds number does appear to affect the results, suggesting that the ratio of transfer functions between two probe sizes has a Reynolds number dependence.

The results presented here will be compared to those found by Sweeney[25] in an effort to confirm and quantify the apparent trends. Additionally, comparisons will be made to the ongoing simulations done by

Chaudhry.[24] The combination of experimental and numerical data should allow for an accurate method of computing the transfer function for the geometry discussed in this paper. This would be an important step in the quest to determine the transfer function for the various geometries of pitot probes, which is crucial when comparing measurements of noise taken in different wind tunnels.

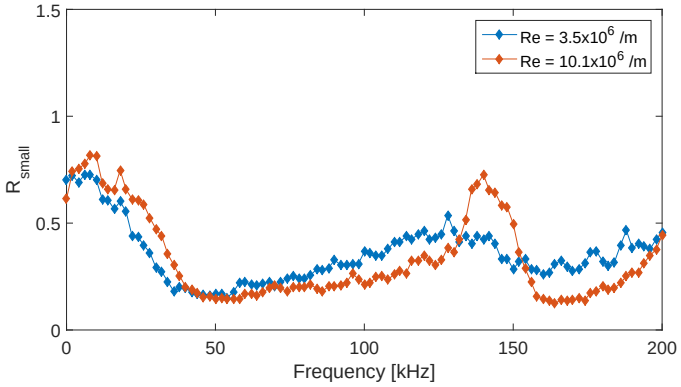

(a) The ratios of the small-sleeve to the no-sleeve PSDs.

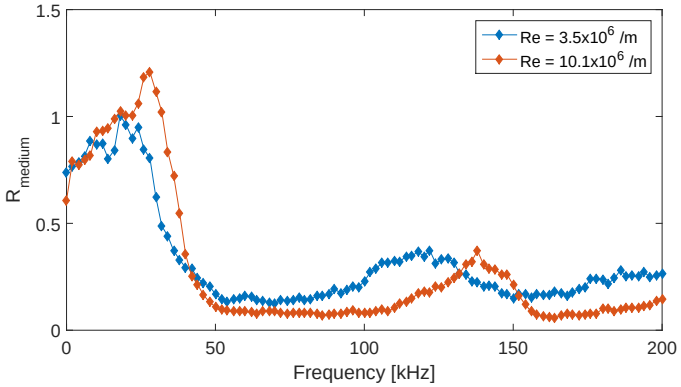

(b) The ratios of the medium-sleeve to the no-sleeve PSDs.

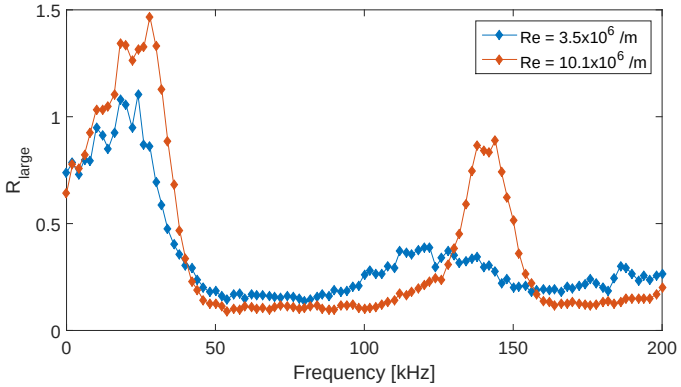

(c) The ratios of the large-sleeve to the no-sleeve PSDs.

Figure 14. The ratios of the PSDs from the probes with the various sleeves to the PSD of the no-sleeve case.

V. Crossflow Secondary Instability Research at Purdue

The crossflow instability is often responsible for boundary-layer transition in three-dimensional flow fields, such as swept wings, lifting bodies, and cones at an angle of attack. On a sharp cone at an angle of attack in hypersonic flow, the shock is stronger near the windward ray than the leeward ray. This creates a circumferential pressure gradient from the wind side to the lee side. The pressure gradient affects the low momentum fluid close to the wall more than the outer flow, creating a crossflow component of the boundary layer flow perpendicular to the outer inviscid flow. The crossflow component has an inflection point and is therefore inviscidly unstable. Crossflow instabilities manifest as either stationary or traveling waves. In low-noise environments like those of flight, stationary waves appear to dominate the transition process.[26]

One path to turbulence is through secondary instabilities of the stationary vortices. The secondary instabilities form in the regions of high shear caused by the upwelling of large stationary vortices. These secondary instabilities have been well studied for low-speed flows mostly on swept wings,[27–31] and are beginning to be measured and computed at high speeds on sharp cones.[32–36] At low speeds, a transition correlation based on N-factors of the secondary instabilities yields better results than one based on the stationary crossflow wave growth alone.[29] This is because the primary instability amplitude saturates well before transition, whereas the secondary instabilities undergo explosive growth just prior to transition. If this remains true at high speeds and a transition-prediction criterion can be formed from high-speed secondary-instability data, it would be a valuable tool for designers of hypersonic vehicles.

Previous research at Purdue University has shown the existence of secondary instabilities (or modulated second-mode waves) on a sharp, circular cone at 6° angle of attack[33,37,38] and measured the nonlinear breakdown of these instabilities.[36] The present work extends that research by measuring the breakdown of the secondary instabilities over a much larger region of the cone and comparing secondary instability amplitude growth to infrared images of the model.

A. Models and Instrumentation

The Modular Cone is a 7° half-angle sharp, circular cone which can use any of multiple inserts with different sensor configurations. Each insert is capable of being rotated to an arbitrary azimuthal position independently of the rest of the cone. A photograph of the Modular Cone System and all of the currently available sensor inserts is shown in Figure 15. For the present work, a new PEEK sensor insert was fabricated for IR imaging. Preliminary IR data has been discussed previously.[44] The PEEK insert can accommodate 24 PCB132 high-frequency pressure sensors and 9 Kulite XCQ-062 transducers. There are 19 PCBs along a single ray, starting at $x = 265.5$ mm and spaced every 6.3 mm. Five additional PCBs are placed off the main ray at 335 mm, 354 mm (x2), and 373 mm (x2). For the present work, the Kulite sensors were not installed. The Modular Cone also supports different configurations of roughness inserts just after the nosetip. For the present work, a dimpled Torlon roughness insert was used with 50 dimples evenly spaced around the azimuth at $x = 50.8$ mm from the nosetip. This is the same insert that was used in previous work at Purdue.[36,37]

B. Infrared Imaging Equipment

An Infratec ImageIR 8300 hp camera was used to image the PEEK. The camera was provided by the University of Notre Dame. According to the manufacturer the camera has a temperature resolution of 0.02 K and an accuracy of ±1° C. The sensor has a 640 x 512 resolution. For the present experiment, images were generally taken at 50 Hz.

A wide-angle 12 mm lens was used, which introduces significant distortion in the image. A basic algorithm to correct for distortion was implemented and the parameters were varied until the edges of the cone were straight lines in the corrected image.

C. New Axial-Azimuthal Maps of Secondary Instability Amplitude

Using the new sensor arrangement on the PEEK insert, the amplitude of the secondary instability can be measured within a large axial-azimuthal area over a series of runs, creating a 'map' of the growth of the

Figure 15. A photograph of the Modular Cone System, including the three available sensor inserts and four of the many roughness inserts.

secondary instability. This technique was previously used successfully with a different sensor arrangement over a smaller measurement region.[39] Figure 16 shows a comparison of the old and new measurement areas overlaid on an IR image of the cone.

1. *Methodology*

Over a series of 25 runs the main ray of PCBs was placed at different azimuthal angles. The series of angles was mostly non-consecutive to reduce systematic error. During the run, the PCBs were sampled at either 2 or 2.5 MHz, depending on the model of oscilloscope to which they were connected. Power spectra of the PCB data were processed from a 0.1 second segment at a predetermined unit Reynolds number using Welch's method, with a frequency resolution of 2.5 kHz. Finally, the RMS amplitude of the fluctuations in a chosen band was calculated by numerically integrating the spectrum and taking the square root. Once all of the runs were complete, the amplitudes from every PCB on the main ray were interpolated to give an axial-azimuthal map of the secondary-instability RMS pressure footprint.

2. *Repeatability*

A more thorough examination of repeatability for the Modular Cone is provided in previous work.[36,44] Figure 17 shows the repeatability data from the present experiment. In Figure 17(a), measured amplitudes from three PCBs at $x = 354$ mm are shown against azimuthal angle. PCB 23 is 6° windward of PCB 18, and PCB 24 is 12° windward of PCB 18. For each PCB, each angle was measured during a different run. The amplitudes match closely except at the peak locations (about 125° and 140°), where the variability is about 30%.

Further upstream, at $x = 335$ mm in Figure 17(b), the amplitudes do not match as closely even in regions away from peaks. There are a number of possible reasons for this discrepancy. At this axial station the

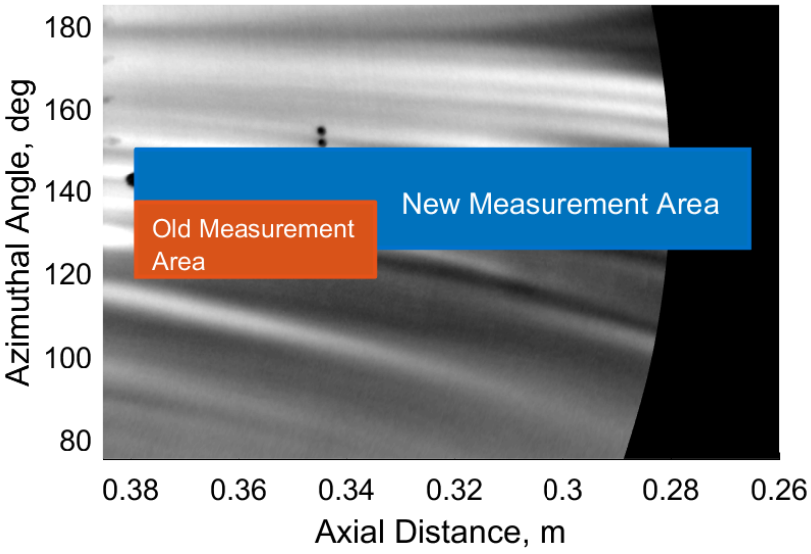

Figure 16. A comparison of the old and new PCB measurement areas. Flow is from right to left. The dark area on the right of the image is part of the cone outside the field of view of the IR camera.

PCBs are about 0.5° wider than at the downstream location. This means that the measurements will be affected by a larger region and the location of the sensing element within the PCB face can more strongly affect the measured amplitude. In addition, it is possible that the discrepancy between the two PCBs is at least partially the result of uncertainty in the factory-supplied PCB calibrations.

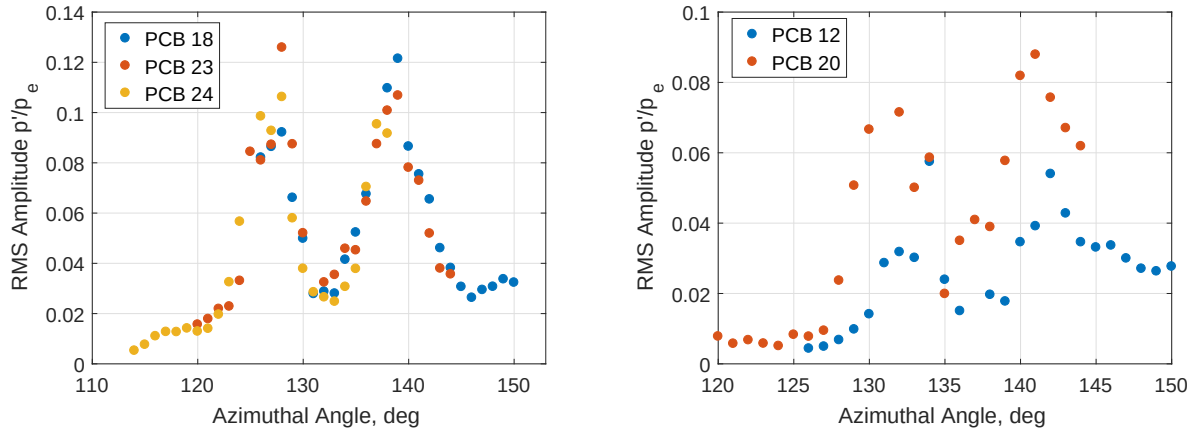

(a) Three PCBs at $x = 354$ mm.

(b) Two PCBs at $x = 335$ mm.

Figure 17. RMS amplitudes in the 250 - 500 kHz band for several different azimuthal angles at two axial positions. $Re_\infty = 12.3 \times 10^6$ **/m.**

3. Results

Figure 18(a) shows an IR image of the PEEK insert with the sensors rotated out of view. The color represents the temperature change from the pre-run state. A method to reduce the temperature-change images to heat

transfer is under development, but not available at present. The camera is centered on the 135° ray. The hot streaks wrapping from wind to lee are likely the result of the thin troughs developing between the stationary vortices. This image can be unwrapped onto an axial-azimuthal plane, as shown in Figure 18(b).

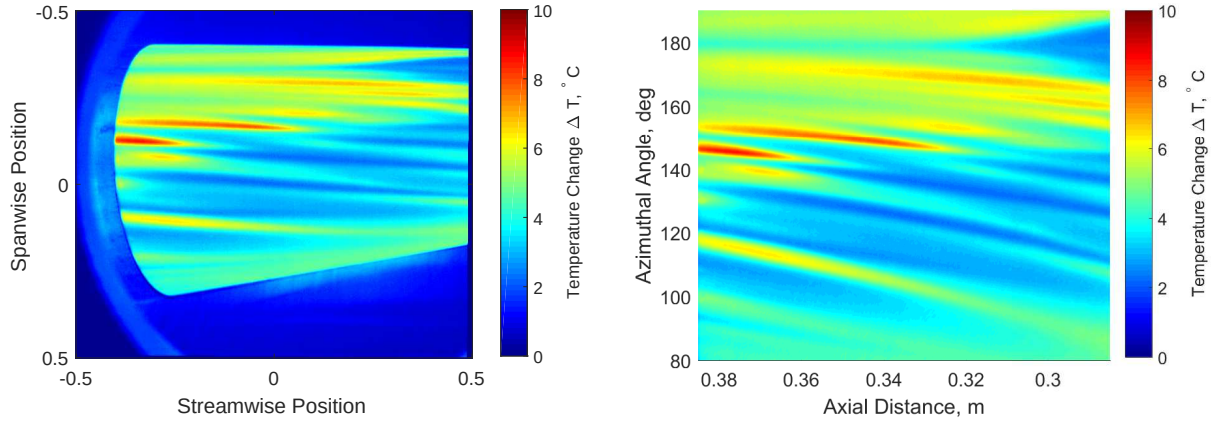

(a) IR image of the PEEK insert at $Re_\infty = 12.1 \times 10^6$ /m.

(b) Unwrapped version of (a).

Figure 18. IR image of the stationary crossflow vortices on the PEEK insert.

As previously described, an axial-azimuthal map of the pressure fluctuations amplitudes can be created over the course of several runs. Data were taken from different times within each run to keep the unit Reynolds number within 0.1×10^6 /m of $Re_\infty = 12.1 \times 10^6$ /m. Figure 19 shows such maps for a low-frequency band (100-270 kHz) and a high-frequency band (250-500 kHz). The data are uniformly spaced every degree from 126° to 150°, and every 6.3 mm axially, except for data missing at 316 mm due to a broken sensor.

In both maps there are clear concentrations of amplitude spaced regularly, and inclined toward the lee ray. The high-frequency map is particularly interesting. For the two central concentrations, there is a very clear growth and decay of the instability, ultimately leading to turbulence. The extent of the growth region is about 50 mm from very low amplitude to nearly turbulent. The low-frequency amplitude concentrations appear to be offset slightly from the high-frequency ones.

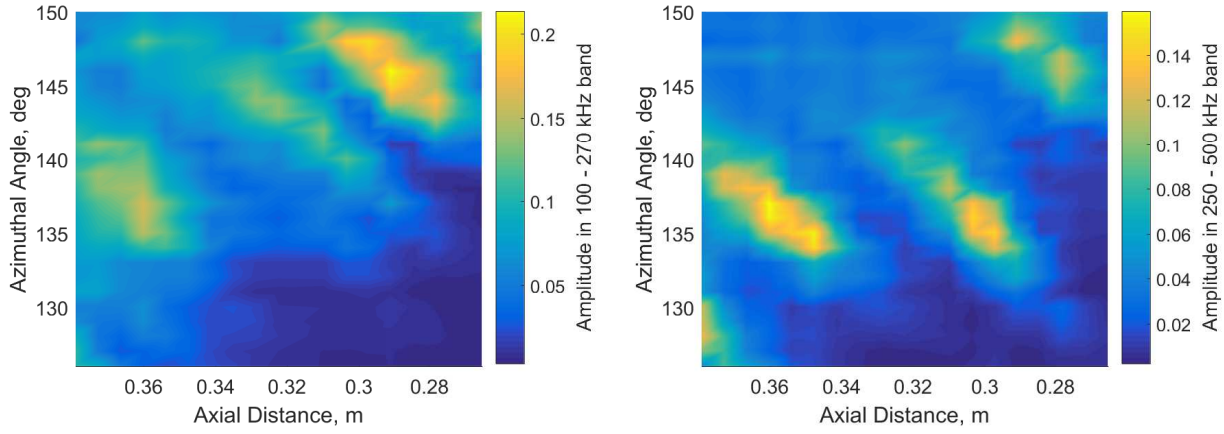

(a) 100-270 kHz.

(b) 250-500 kHz

Figure 19. Measured fluctuation amplitudes in a low- (a) and high-frequency (b) band.

The contours from the high-frequency amplitude map can be extracted and overlaid on the unwrapped IR image. This is shown in Figure 20. The high-frequency concentrations are directly on top of streaks in the IR. Interestingly, after the high-frequency instability amplitude has peaked and begun to decay, new streaks appear in the IR offset leeward by about half the wavelength of the stationary vortices. These streaks rapidly increase in temperature. From the spectra, these streaks appear to be in turbulent or nearly turbulent flow. These new streaks may indicate the breakdown of the stationary vortices and the onset of turbulent flow, whereas the hot streaks upstream are due to the thinning of the boundary layer between stationary vortices.

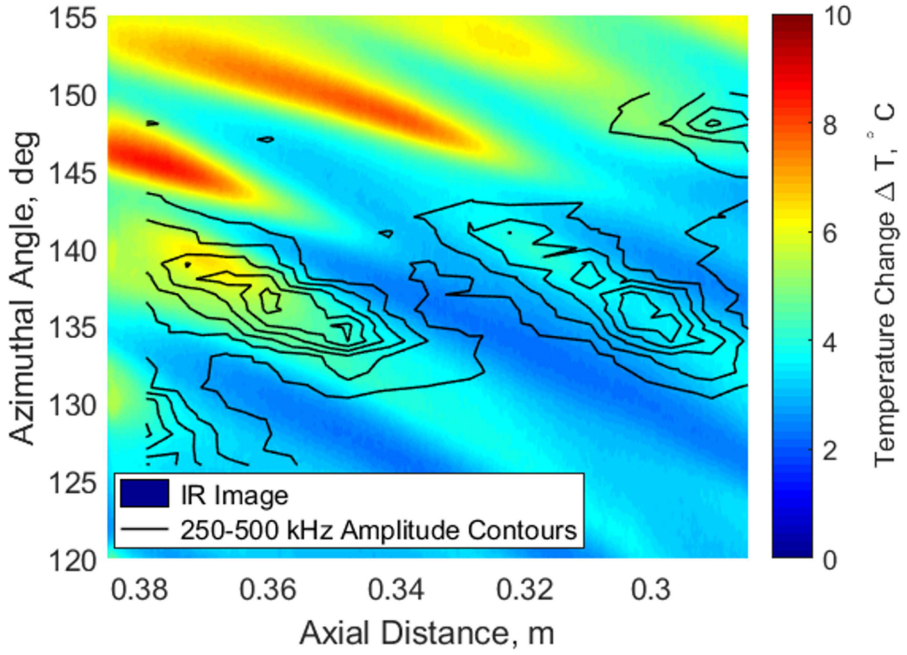

Figure 20. Contours of the 250-500 kHz amplitude overlaid on the IR image. Hot streaks appearing at 145° and about 0.32 m and 0.36 m may be the stationary vortices breaking down to turbulence.

Figure 21 shows the paths of the peaks of the two most-central hot streaks. The black circles are the locations of PCB measurements. Figure 22 show some power spectra from PCB measurements along each streak. The spectra from both streaks show that the flow is nearly turbulent at the end of the measurement region.

In Figure 23, the amplitudes of the high-frequency fluctuations at these PCB locations are compared to the amplitude of the streak computed from the IR. The streak amplitude is defined as in Edelman,[36]

$$A = 2\,\frac{\Delta T_{peak} - \Delta T_{min}}{\Delta T_{peak} + \Delta T_{min}}, \tag{5}$$

where ΔT is the difference in temperature between the measurement and the pre-run state.

Note that in Reference 36, the definition of the amplitude uses wall heat-transfer instead of temperature change. Methods for inferring heat transfer from IR images are under development, but none were complete at the time of this writing.

Figure 23(a) shows the amplitude development for the upper streak, Streak 1. This streak extends from the beginning of the IR at about 290 mm to about 320 mm, where it disappears or merges with a rapidly growing hot-streak half a wavelength leeward (see Figure 20). The high-frequency fluctuation grows rapidly at the same time as the streak, but reaches peak amplitude (about 15%) about 200,000 in Re before the streak reaches peak amplitude. The fluctuation amplitude then decays over the course of about $Re = 400,000$

to near turbulence. The peak streak amplitude is about 0.5, meaning the peak-to-peak magnitude of the temperature change for that stationary vortex is about one half the local mean temperature increase from the pre-run state (i.e., if the surface of the cone in that region were on average 5 °C hotter than before the run, the peak-to-peak magnitude of the streaks would be about 2.5 °C).

Figure 23(b) shows the same quantities for Streak 2, which extends from 290 mm to the end of the IR image, about 385 mm. In this case, the amplitude of the streak grows much more slowly, but again the fluctuation amplitude and the streak amplitude reach their peaks very close to one another (with the fluctuation peak preceding the streak peak). The peak fluctuation amplitude is roughly the same on both Streak 1 and Streak 2, but the streak amplitude is about 50% higher on Streak 2.

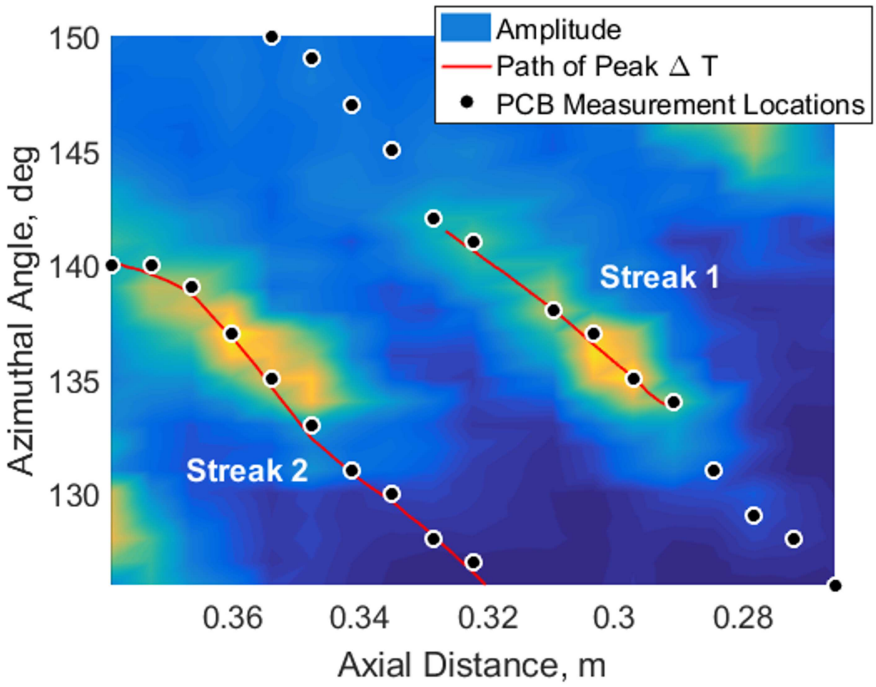

Figure 21. PCB measurement locations compared to the paths of the peak temperature change from IR. The background is the 250-500 kHz amplitude map.

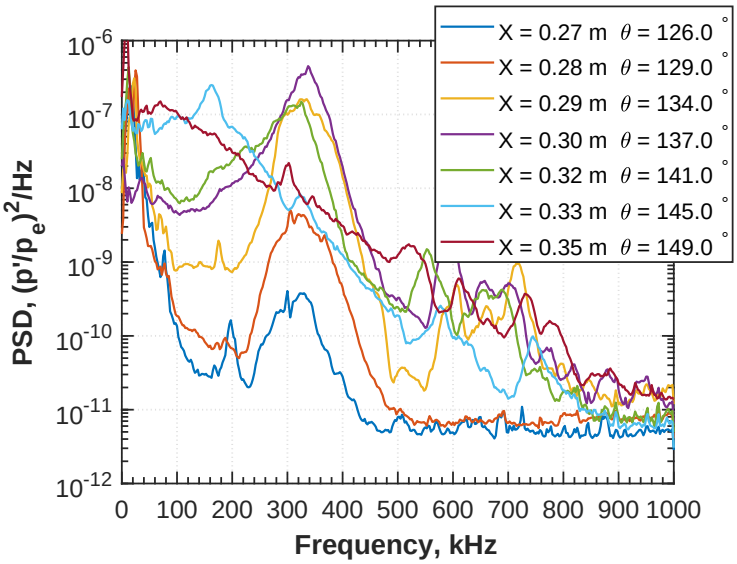

(a) Power spectra along Streak 1.

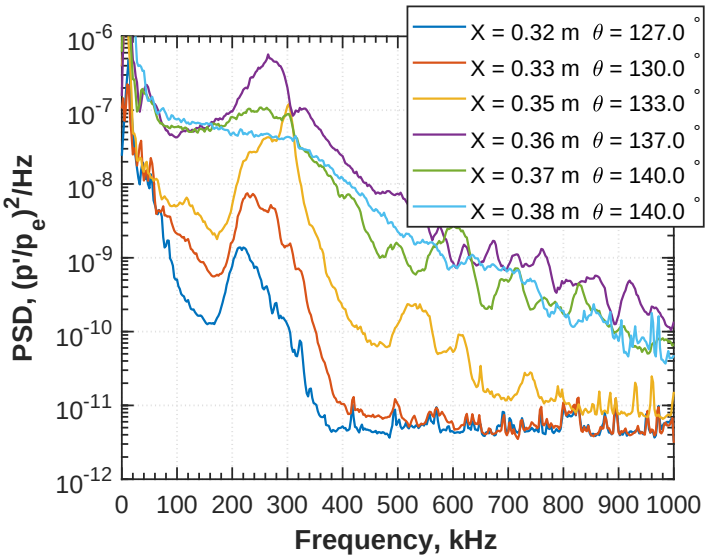

(b) Power spectra along Streak 2.

Figure 22. Power spectra from the indicated PCB measurements along Streaks 1 and 2. $Re_\infty \approx 12.3 \times 10^6/m$.

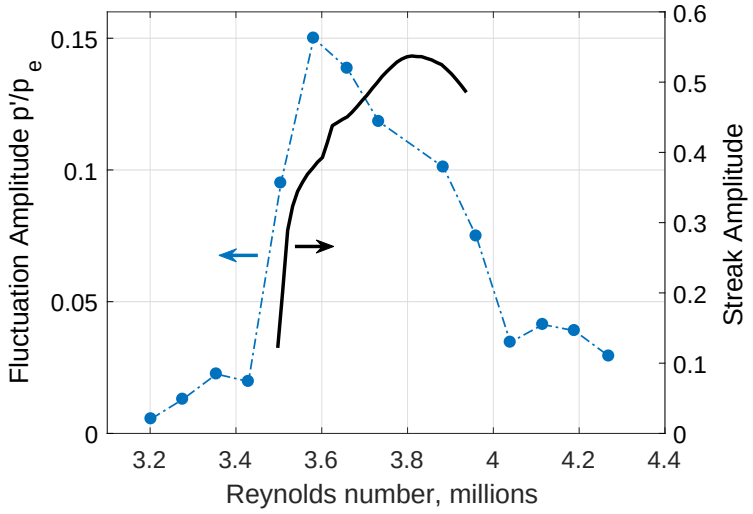

(a) Amplitudes along Streak 1.

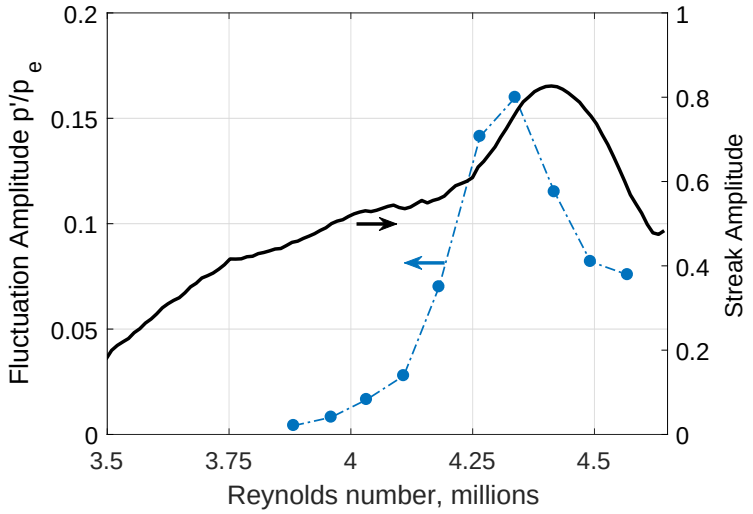

(b) Amplitudes along Streak 2.

Figure 23. Streak and high-frequency fluctuation amplitude development compared to axial-location Reynolds number. Note that the edge of the IR data is at 290 mm, or about $Re = 3.5 \times 10^6$.

VI. Boundary-Layer Transition Measurements Through a Finite Span Compression Corner

Boundary-layer flow approaching a ramp or control surface on a hypersonic vehicle is subjected to an adverse pressure gradient due to the shock wave at the compression corner. The adverse pressure gradient will retard the incoming boundary layer and, if strong enough, cause separation. This phenomenon is categorized as a shock wave-boundary layer interaction (SBLI). At these locations, laminar-turbulent transition commonly occurs within the free-shear layer and can lead to some of the highest heating loads on the surface.[40] Gaining a basic understanding of how the free-shear layer affects the natural transition on a body will help in designing maneuverable high speed vehicles. Measurements of transitional SBLI are exceedingly difficult due to the inherent three-dimensionality and non-linear processes.[41,42] However, with modern advancements in computational capability and experimental techniques there is a renewed interest in transitional SBLI.

A. Model

Several models based on a design by Oberkampf et al. were designed and fabricated for use within the BAM6QT.[43] The original model designed for the BAM6QT had the same relative slice and flap positions as the Oberkampf cone but had a 7° half angle instead of 10°. Initial experiments have been completed over the past year.[36,44] However, this model did not have a ramp long enough to allow for measurements of the boundary layer post-reattachment. Since post-reattachment measurements are needed for determining the effect of the free shear layer on transition, a new model was designed. The new model has a longer ramp and can be seen in Figure 24. The model consists of a nosetip with a 110 micrometer radius followed by a 7° half angle cone. At 0.248m downstream of the nosetip axially, a slice is machined on the cone. This slice is parallel with the model's axis and provides the upstream surface for the compression corner. Four interchangeable ramps are 0.091m long and have deflection angles of 5°, 10°, 15°, and 20°. These ramps span the width of the slice at the upstream edge.

The model has 12 holes for PCB132A31 fast pressure sensors centered on the ramp and slice. Seven of these sensor holes are located on the ramp and five of them are located on the slice. A precision angle-of-attack adapter designed by Brandon Chynoweth was used to ensure the tests were conducted at 0.0° angle of attack. TSP was applied to the surface of the model and calibrated using a Schmidt-Boelter heat transfer gauge.

The angle-of-attack was checked by comparing PCB power spectra at 90° azimuthal intervals around the cone. The sensor locations aligned with 4 set screws on the sting adapter that could be adjusted to make finely controlled adjustments to the angle-of-attack. Figure 25 shows the azimuthal PCB's in degrees away from the centerline array of PCB's. The cases were run at Re/m=7.9×10^6/m in noisy flow. These conditions provided large amplitude instability waves that could be used for zeroing out the model angle. It was assumed that higher frequency peaks corresponded to thinner boundary layers located on the windward side of the model and vica-versa. Once the initial position was established (Figure 25(a)), the set crews were given a full turn and the case was rerun(Figure 25(b)). This was repeated until the peaks overlapped each other within 3 kHz(Figure 25(c)). At this point the model was considered to be at 0.0° angle-of-attack.

B. Current Results

TSP images and PCB pressure fluctuations were collected for numerous Reynolds numbers within the BAM6QT. All tests were conducted with the 20° ramp. The model was tested under quiet and noisy conditions to observe the effect of freestream acoustic noise on the interaction. Additionally, an attempt was made to make measurements on the slice and ramp under fully laminar, transitional, and turbulent boundary-layer flow. This would help to define and clarify the capabilities of the model and define flow conditions for possible computational comparisons.

Experiments were scrutinized using two metrics. Firstly, by observing the location of transitional heating on the cone portion of the model. If an increase in heat transfer was observed off the slice and ramp, then it was assumed the boundary layer was naturally transitioning under the experimental conditions.

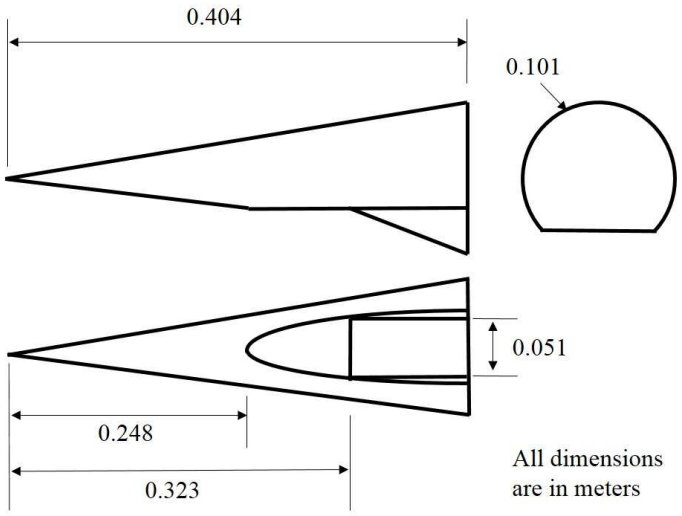

Figure 24. Schematic of the cone with slice and ramp.

Examples of this can be seen in Figure 26. The white lines correspond to the locations on the cone where the heating increases to over double the upstream value. To further illustrate this, Figure 27 shows heat transfer contours at 4 kW/m^2, approximately double the heating present upstream of the slice. These plots illustrate the issue with the cone boundary layer transitioning and are used to ensure the boundary layer present on the flap is not being influenced by Reynolds number effects on the cone boundary layer. This is important since pre-separation boundary-layer state has a large effect on separation and reattachment. Secondly, the boundary-layer state post-reattachment was observed using PCB surface-pressure measurements. Knowing whether the boundary layer reattachment was laminar, transitional or turbulent will help to pinpoint the axial transition location and whether it is within or near the SBLI.

Figure 28 shows the heat transfer present on the ramp at numerous Reynolds numbers in noisy flow. The heat transfer scales in Figure 28 are adjusted to see the highest contrast possible. For all images shown the ramp begins at x = 0.316m axially downstream of the nosetip. Figures 28(a)-28(f) show reattachment in noisy flow for cases where the transition front, located azimuthally off the slice, is downstream of the compression corner. To illustrate this, Figure 26(a) shows the heat transfer over the full cone for the Re_∞=5.9$\times$10^6/m case. The white lines on the image are interpreted as a transition front and they are only present downstream of the compression corner. The heat transfer patterns in Figures 28(a)-28(f) show asymmetry of the surface heating and therefore an asymmetry in reattachment location. The reason for this is currently unknown, however it could be due to roughness non-uniformities or residual angle-of-attack. For these cases, streaks of heating are present on the edges of the ramp where the reattachment is heavily curved. There are no streamwise streaks of heating post-reattachment between those on the edges. This is unlike previous experiments where streamwise streaks of heating have been measured across the model span under noisy conditions.[41,45–47]

In order to check if is re-attachment is transitional, Figure 29 shows the PCB power spectra of the second to last PCB present on the ramp for all the Reynolds numbers shown in Figure 28. This sensor was chosen since it is the furthest upstream sensor that is not inside the separation for every case. The lowest Reynolds number case is shown in Figure 28(a) and appears to reattach laminar. This is evidenced by the low spectral power and lack of features on the PSD trace. The Re_∞=2.1$\times$10^6/m to 3.6$\times$10^6/m cases (Figures 28(b)-28(e)) show a boundary layer at reattachment that is transitional or unstable with broadband instabilities. This inference is based on the broadband increase in power of the power spectra as the Reynolds number increases. This suggests that for these Reynolds numbers and test cases, the free shear layer is unstable enough to transition off the surface of the model.

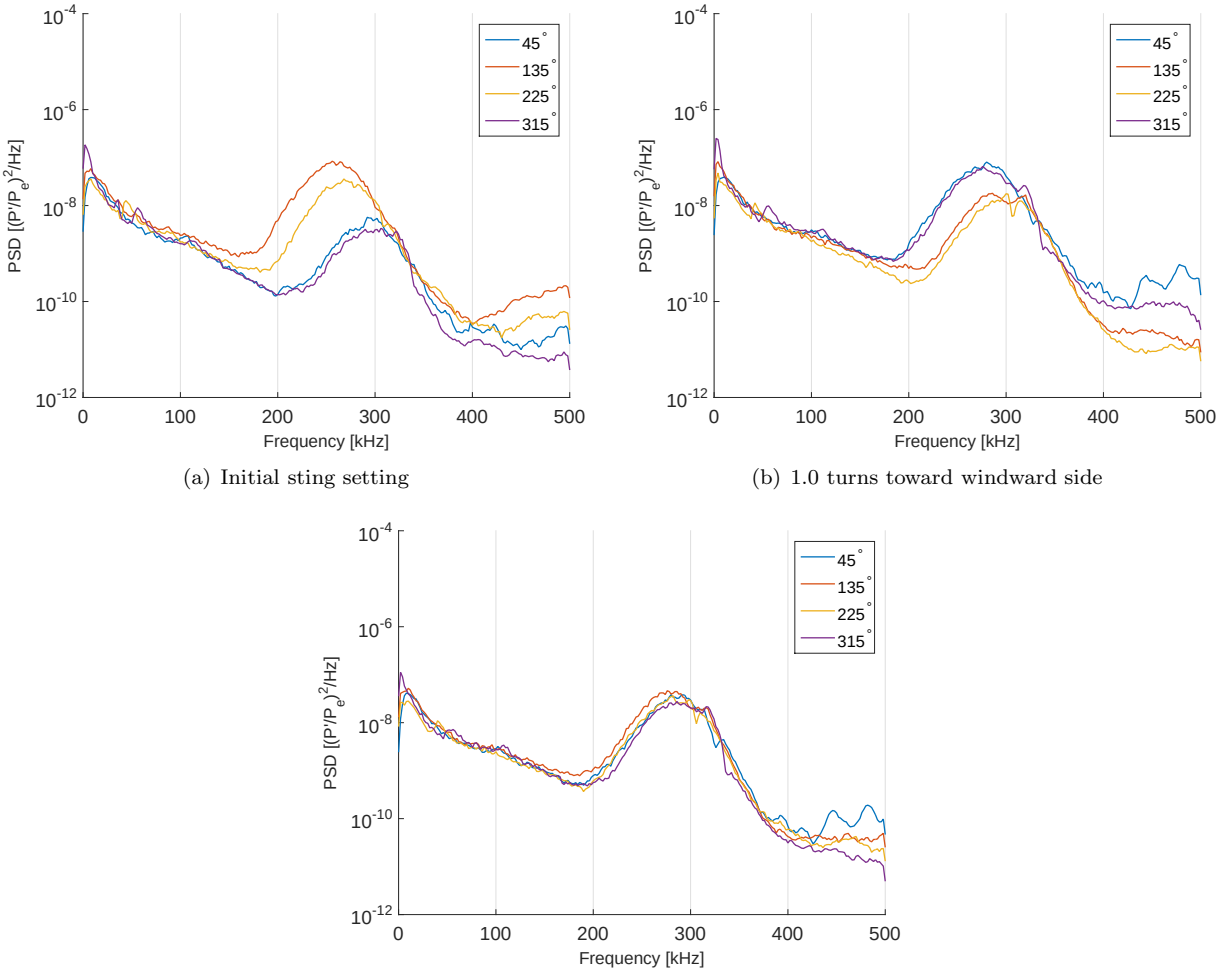

(a) Initial sting setting

(b) 1.0 turns toward windward side

(c) 1.5 turns toward windward side

Figure 25. PCB Power spectra over multiple runs with sting adjustments to ensure 0° angle-of-attack.

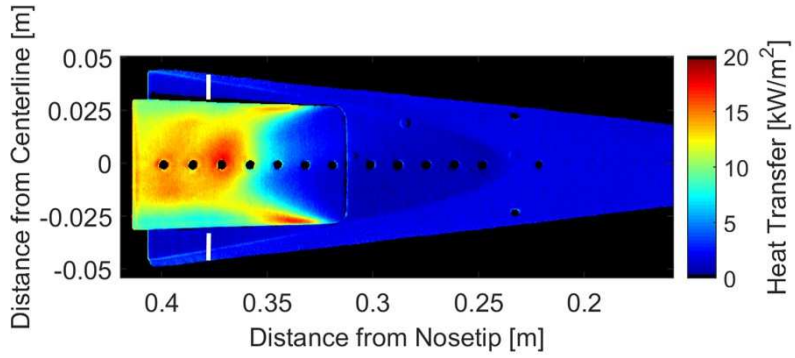

(a) Re_∞=5.9×10^6/m

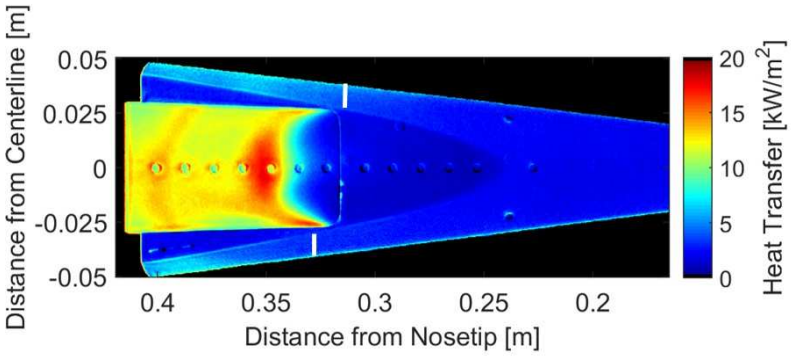

(b) Re_∞=9.4×10^6/m

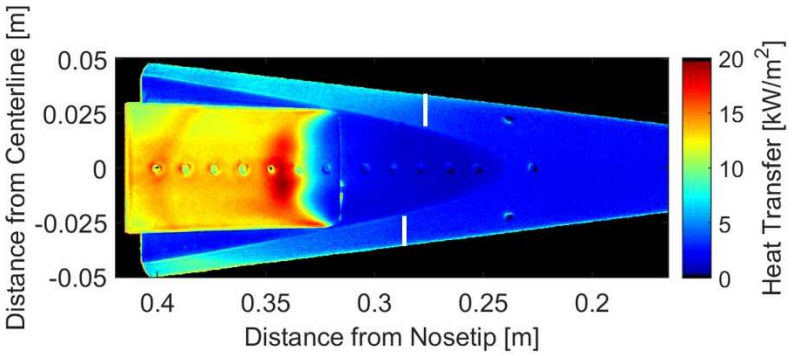

(c) Re_∞=10.9×10^6/m

Figure 26. TSP of the full cone at varying unit Reynolds number in noisy flow. Flow is from right to left. The white lines are the approximate start location of the off-slice heat-transfer increase due to transition.

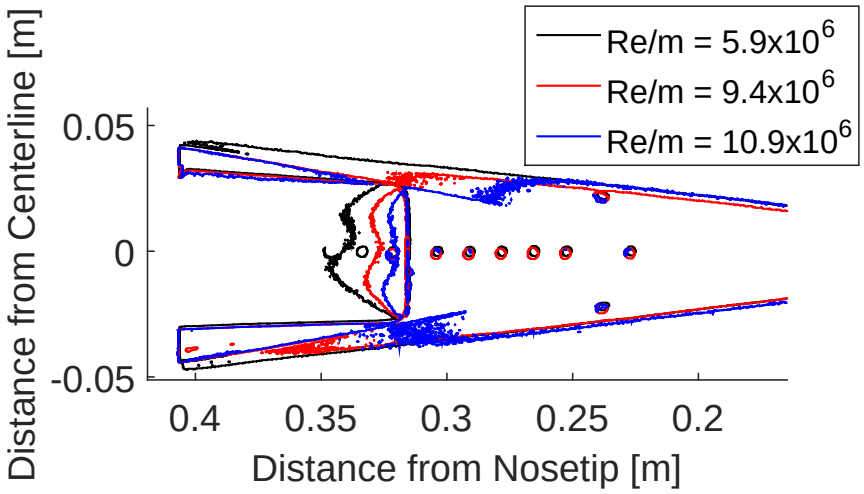

Figure 27. Heat transfer contours at various unit Reynolds number. The contour is set to trace out lines of 4 kW/m^2.

For Re_∞=7.0×10^6/m and above (Figures 28(g)-28(j)) the size of the separation bubble is reducing as the Reynolds number increases. This could be due to the pre-separation boundary-layer transitioning. Transition increases the boundary layer's momentum transfer and thus it is more resistant to the adverse pressure gradient and can resist separation. Figures 26(b), 26(c), and 27 show the perceived transition front on the cone, labeled as white lines or contours moving upstream as the Reynolds number increases. The movement of transition is believed to be the reason for the change in separation length and for Reynolds number greater than 7.0×10^6/m, Figure 29 shows turbulent spectra downstream of re-attachment. Thus for noisy flow, boundary-layer transition on the flap should be interpreted carefully due to the effects of Reynolds number on the cone boundary-layer transition.

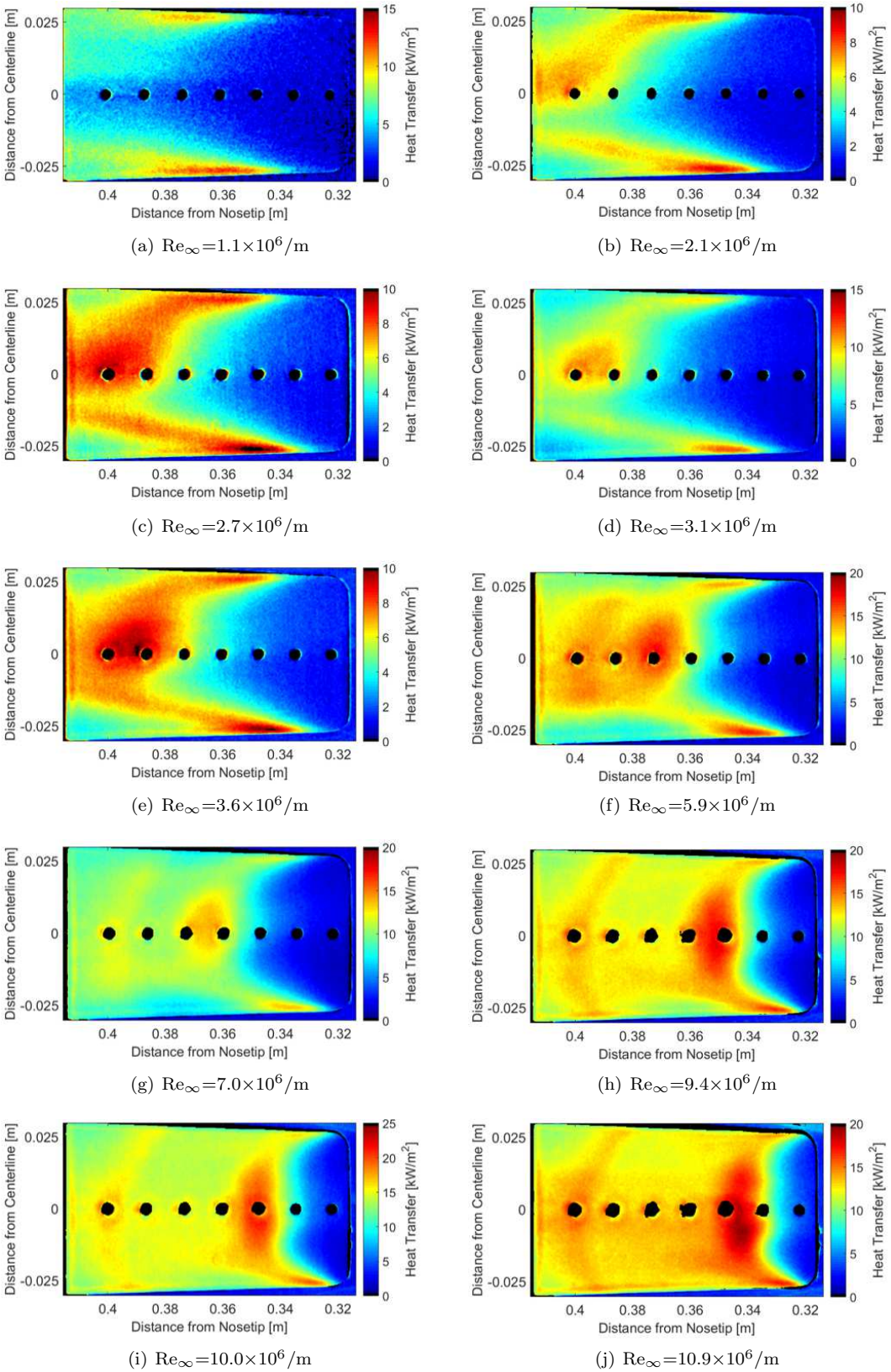

(a) Re_∞=1.1×10^6/m

(b) Re_∞=2.1×10^6/m

(c) Re_∞=2.7×10^6/m

(d) Re_∞=3.1×10^6/m

(e) Re_∞=3.6×10^6/m

(f) Re_∞=5.9×10^6/m

(g) Re_∞=7.0×10^6/m

(h) Re_∞=9.4×10^6/m

(i) Re_∞=10.0×10^6/m

(j) Re_∞=10.9×10^6/m

Figure 28. TSP of the ramp at varying unit Reynolds number in noisy flow. Flow is from right to left and the ramp begins at x = 0.316m.

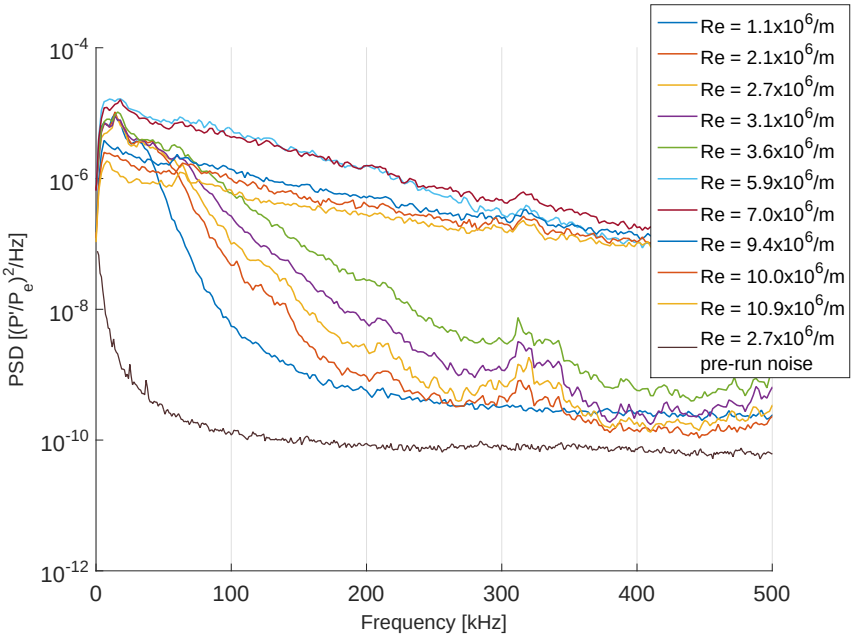

Figure 29. PSD's for the second to last PCB on the ramp in noisy flow. This PCB is located 0.375m axially downstream of the nosetip.

Figure 30 shows TSP images of the ramp for numerous Reynolds numbers in quiet flow. It should be noted that the heat-transfer scales on these images are again adjusted for maximum contrast. For all the cases shown, evidence of a transition front located on the cone azimuthally off the slice was not observed. As a result, the reattachment location does not significantly change over the course of the Reynolds number sweep. Figure 30(a) shows a case where the boundary layer at the centerline downstream of reattachment. This can be observed in Figure 31, where the Re_∞=2.0×10^6/m trace exhibits low spectral power across all frequencies. This is nearly double the Reynolds number of the laminar case in a noisy flow environment. Above this Reynolds number (Figures 30(b)-30(h)), the PCB's show a transitional power spectra or one with broadband instabilities downstream of reattachment and the intensity of the heat transfer increases accordingly.

The quiet-flow heat-transfer structure post-reattachment is different than in the noisy flow. For all tested conditions, regions of high heating were present near the edges of the ramps where reattachment heating curves upstream. At low Reynolds numbers (Figures 30(a)-30(c)), another region of heating is present at roughly 0.01m off the centerline. The reason for the region to be present in this location, or the reason for a lack of other streaks is not known. As the Reynolds number increases this region widens and produces a local maxima of heat transfer (Figures 30(d)-30(f)). At the two highest Reynolds numbers (Figures 30(g) and 30(h)), the upstream portion of this heating region narrows and becomes more streak-like near 0.01m off the centerline. The cause of this is currently not known.

Future experiments will focus on obtaining measurements of instability growth through the separation with varying transition locations. Additionally, off-centerline measurements will be completed and can capture the surface pressure footprint of post-reattachment heating streaks. The capability of running a plasma perturber on the model is being investigated as well.

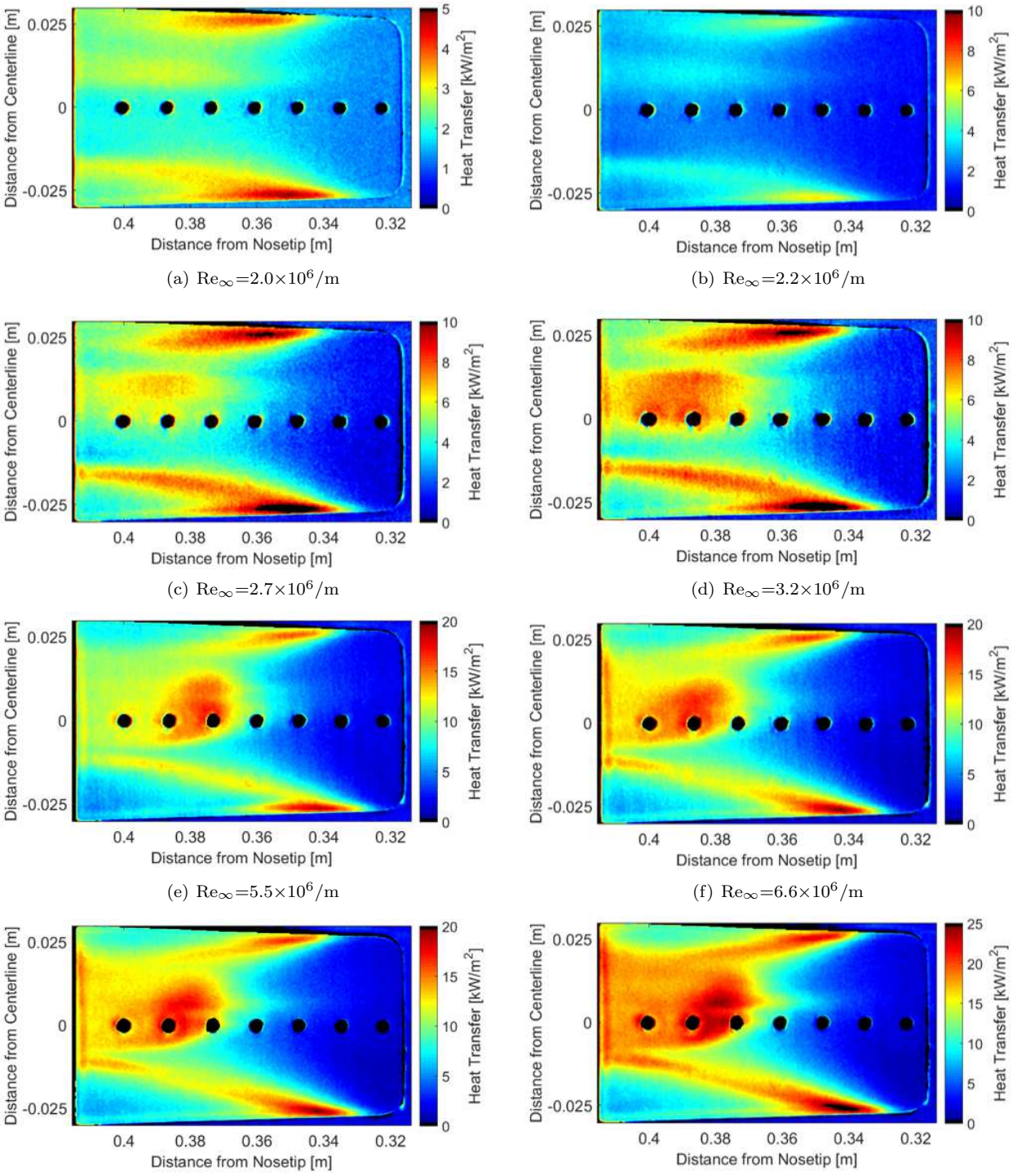

(a) Re_∞=2.0×10^6/m

(b) Re_∞=2.2×10^6/m

(c) Re_∞=2.7×10^6/m

(d) Re_∞=3.2×10^6/m

(e) Re_∞=5.5×10^6/m

(f) Re_∞=6.6×10^6/m

(g) Re_∞=7.9×10^6/m

(h) Re_∞=9.2×10^6/m

Figure 30. TSP of the ramp at varying unit Reynolds number in quiet flow. Flow is from right to left.

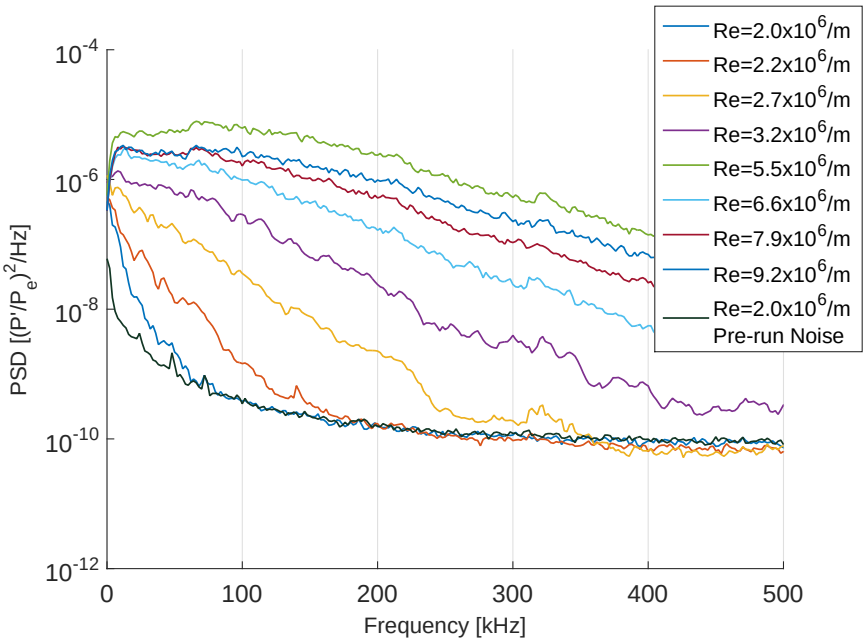

Figure 31. PSD's for the second to last PCB on the ramp in quiet flow. This PCB is located 0.375m axially downstream of the nosetip.

VII. Conclusion

1. A study of boundary-layer edge-detection methods was performed. A method based on the return of the total enthalpy to within a certain percent of the freestream value would be used for future edge-detection computations performed on the flared cone geometry. Measurements with an optical profiler were taken of a RIM inserts, and experimental results showed the relationship between the second-mode magnitudes measured and the heating pattern. A maximum second-mode magnitude of almost 27% was measured. This maximum occurred upstream of where intermittency calculations and broadband spectral filling indicate transition begins. Experiments to compare with computations are ongoing.

2. It is too early to make definitive statements about the trends observed in the pitot measurements taken using various sleeves. However, it is clear that the size of the probe does have an effect on the measured pressure fluctuations. Furthermore, the ratio between the PSDs resulting from two different probe sizes appears to be Reynolds-number dependent. Future work on this topic will include comparisons of experimental results to simulations. Since the transfer function cannot be measured directly, the ratio method presented here may be a valuable tool for comparing experimental results to simulations. Those comparisons will be crucial for correctly determining the transfer function of a given probe geometry.

3. A new Modular Cone insert allows the high-fidelity measurement of the spatial location of secondary instabilities on a 7° cone at 6° angle of attack. The new measurements show that high-frequency instabilities occur coincidentally with troughs of the stationary vortices. Near breakdown, new streaks appear in the IR offset by one-half of the wavelength of the stationary vortices. The new measurement technique also allows better measurements of the growth and breakdown of the stationary waves and secondary instabilities simultaneously.

   Future experiments will use different roughness inserts with small variations in roughness wavenumber to determine the wavenumber's effect on the nonlinear breakdown of the secondary instabilities. In

addition, quantitative comparisons will be made between these experimental data and computations from NASA Langley and Texas A&M.

4. Experiments were completed in order to characterize the flow over an inherently three-dimensional model of a cone with a slice and ramp. The current experiments have shown that it is possible to design a geometry that facilitates measurements of the boundary layer post-reattachment. The range of Reynolds numbers possible within the BAM6QT allows for measurements of laminar and transitional boundary layers downstream of reattachment in quiet and noisy flow. Additionally, it seems to be possible to measure turbulent SBLI within noisy flow conditions. Under noisy flow, streamwise streaks were only present on the edges of the ramp within the heat transfer images for laminar, transitional, or turbulent flow. Under quiet flow conditions, streamwise streaks were present downstream of reattachment for all Reynolds numbers. Future experiments will focus on the breakdown of instabilities through the separated region and possible electronic perturber measurements.

VIII. Acknowledgements

Much of this research is funded by the Air Force Office of Scientific Research under grant number FA9550-12-1-0167. The research by Brandon Chynoweth and Joshua Edelman was conducted with Government support under and awarded by DoD, Air Force Office of Scientific Research, National Defense Science and Engineering Graduate (NDSEG) Fellowship, 32 CFR 168a. Brandon Chynoweth would like to thank Dr. Joe Jewell for providing an enlightening article that led to a better understanding of the history of boundary-layer edge detection methods in hypersonic flows. Additionally, the help provided by Heath Johnson on the inner workings of STABL were invaluable. Josh Edelman would like to thank Dr. Tom Juliano, Harrison Yates, and Carson Running of the University of Notre Dame for their help in setting up and using the Notre Dame IR camera.

References

[1]Lin, T., "Influence of Laminar Boundary-Layer Transition on Entry Vehicle Designs," *Journal of Spacecraft and Rockets*, Vol. 45, No. 2, March–April 2008, pp. 165–175.

[2]John D. Anderson, Jr., *Hypersonic and High-Temperature Gas Dynamics*, AIAA Education Series, 2nd ed., 2006.

[3]Chou, A., Wheaton, B. M., Ward, C. A., Gilbert, P. L., Steen, L. E., and Schneider, S. P., "Instability and Transition Research in a Mach-6 Quiet Tunnel," *AIAA Paper 2011-0283*, January 2011.

[4]Hofferth, J. W. and Saric, W. S., "Boundary-Layer Transition on a Flared Cone in the Texas A&M Mach 6 Quiet Tunnel," *AIAA Paper 2012-0923*, January 2012.

[5]Schneider, S. P., "Development of Hypersonic Quiet Tunnels," *Journal of Spacecraft and Rockets*, Vol. 45, No. 4, July-August 2008, pp. 641–664.

[6]Zhang, C.-H., Tang, Q., and Lee, C.-B., "Hypersonic Boundary-Layer Transition On A Flared Cone," *Acta Mechanica Sinica*, Vol. 29, No. 1, February 2013, pp. 48–54.

[7]Zhu, Y., Zhang, C., Chen, X., Yuan, H., Wu, J., Chen, S., Lee, C., and el Hak, M. G., "Transition in Hypersonic Boundary Layers: Role of Dilatational Waves," *AIAA Journal*, Vol. 54, No. 10, October 2016, pp. 3039–3049.

[8]Dundian, G., Shihe, Y., and Xiaoge, L., "Design and Performance of a Hypersonic Quiet WInd Tunnel at NUDT," *AIAA Paper 2017-2305*, March 2017.

[9]Steen, L. E., *Characterization and Development of Nozzles for a Hypersonic Quiet Wind Tunnel*, Master's Thesis, Purdue University School of Aeronautics & Astronautics, West Lafayette, IN, December 2010.

[10]Marineau, E. C., "Prediction Methodology for Second-Mode-Dominated Boundary-Layer Transition in Wind Tunnels," *AIAA Journal*, Vol. 55, No. 2, February 2017.

[11]Bertin, J. J., *Hypersonic Aerothermodynamics*, American Institute of Aeronautics and Astronautics, Inc., 370 L'Enfant Promenade, SW, Washington, DC 20024-2518, 1994, Pages: 114-120, 337-338.

[12]Jewell, J. S. and Kimmel, R. L., "Boundary-Layer Stability Analysis for Stetson's Mach 6 Blunt-Cone Experiments," *Journal of Spacecraft and Rockets*, Vol. 54, No. 1, January-February 2017, pp. 258–265.

[13]Stetson, K., "Nosetip Bluntness Effects on Cone Frustum Boundary Layer Transition in Hypersonic Flow," *AIAA Paper 1983-1763*, July 1983.

[14]J.C. Adams Jr., W.R. Martindale, A.W. Mayne Jr., and E.O. Marchand, "Real-Gas Scale Effects on Shuttle Orbiter Laminar Boundary-Layer Parameters," *Journal of Spacecraft and Rockets*, Vol. 14, No. 5, May 1977, pp. 273–279.

[15]Levine, J., "Finite Difference Solution of the Laminar Boundary Layer Equations Including Second-Order Effects," *AIAA Paper 1968-0739*, June 1968.

[16]Berry, S. A., II, H. H. H., and Wurster, K. E., "Effect of Computational Method on Discrete Roughness Correlations for Shuttle Orbiter," *Journal of Spacecraft and Rockets*, Vol. 43, No. 4, July-August 2006.

[17]Robarge, T. W., *Laminar Boundary-Layer Instabilities on Hypersonic Cones: Computations for Benchmark Experiments*, Master's Thesis, Purdue University School of Aeronautics & Astronautics, West Lafayette, IN, August 2005.

[18]Fedorov, A., "Transition and Stability of High-Speed Boundary Layers," *Annual Review of Fluid Mechanics*, Vol. 43, 2011, pp. 79–95.

[19]Wheaton, B. M., "Boundary Layer Stability on Circular-Arc Geometries at Mach 6," Tech. rep., Purdue University AAE 624 Final Report, December 2008.

[20]Wheaton, B., "Personal Communication via E-Mail," 2 February 2017, The Johns Hopkins Applied Physics Laboratory.

[21]Marineau, E. C., "Personal Communication via E-Mail," 21 September 2016, Arnold Engineering Development Center Tunnel 9.

[22]Casper, K. M., Beresh, S. J., Henfling, J. F., Spillers, R. W., and Pruett, B. O., "Toward Transition Statistics Measured on a 7-Degree Hypersonic Cone for Turbulent Spot Modeling," *AIAA Paper 2014-0427*, January 2014.

[23]Chaudhry, R. S. and Candler, G. V., "Computing Measured Disturbances for Hypersonic Pitot Probes," 2016, Under review at AIAA Journal.

[24]Chaudhry, R., private communication, February 2017.

[25]Sweeney, C. J., *Characterization of a Hypersonic Quiet Wind Tunnel Nozzle*, Master's thesis, Purdue University, School of Aeronautics and Astronautics, West Lafayette, Indiana, December 2016.

[26]Deyhle, H. and Bippes, H., "Disturbance Growth in an Unstable Three-Dimensional Boundary Layer and Its Dependence on Environmental Conditions," *Journal of Fluid Mechanics*, Vol. 316, 1996, pp. 73–113.

[27]Kohama, Y., Saric, W., and Hoos, J., "A High-Frequency, Secondary Instability of Crossflow Vortices that Leads to Transition," *Proceedings of the Royal Aeronautical Society Conference on Boundary Layer Transition and Control*, February 1991, pp. 4.1–4.13, Cambridge, U.K, pages 4.1-4.13, February 1991.

[28]Malik, M., Li, F., and Chang, C.-L., "Nonlinear Crossflow Disturbances and Secondary Instabilities in Swept-Wing Boundary Layers," *IUTAM Symposium on Nonlinear Instability and Transition in Three-Dimensional Boundary Layers*, edited by P. W. Duck and P. Hall, Kluwer Academic Publishers, 1996, pp. 257–266, Manchester, U.K.

[29]Malik, M., Li, F., Choudhari, M., and Chang, C.-L., "Secondary Instability of Crossflow Vortices and Swept-Wing Boundary-Layer Transition," *Journal of Fluid Mechanics*, Vol. 399, 1999, pp. 85–115.

[30]White, E. and Saric, W., "Secondary Instability of Crossflow Vortices," *Journal of Fluid Mechanics*, Vol. 525, 2005, pp. 275–308.

[31]Li, F., Choudhari, M., Carpenter, M., Malik, M., Chang, C.-L., and Streett, C., "Control of Crossflow Transition at High Reynolds Numbers Using Discrete Roughness Elements," *AIAA Journal*, Vol. 54, No. 1, January 2016.

[32]Craig, S. and Saric, W., "Crossflow Instability in a Hypersonic Boundary Layer," *Journal of Fluid Mechanics*, Vol. 808, December 2016, pp. 224–244.

[33]Ward, C., Henderson, R., and Schneider, S., "Possible Secondary Instability of Stationary Crossflow Vortices on an Inclined Cone at Mach 6," *AIAA Paper 2015-2773*, June 2015.

[34]Moyes, A., Paredes, P., Kocian, T., and Reed, H., "Secondary Instability Analysis of Crossflow on a Hypersonic Yawed Straight Circular Cone," *AIAA Paper 2016-0848*, January 2016.

[35]Li, F., Choudhari, M. M., Paredes, P., and Duan, L., "High-frequency Instabilities of Stationary Crossflow Vortices in a Hypersonic Boundary Layer," *Physical Review Fluids*, Vol. 1, No. 053603, September 2016.

[36]Edelman, J., *Secondary Instabilities of Hypersonic Stationary Crossflow Waves*, Master's thesis, Purdue University, West Lafayette, IN, December 2016.

[37]Ward, C., *Crossflow Instability and Transition on a Circular Cone at Angle of Attack in a Mach-6 Quiet Tunnel*, Ph.D. thesis, Purdue University, December 2014.

[38]Henderson, R., *Crossflow Transition at Mach 6 on a Cone at Low Angles of Attack*, Master's thesis, Purdue University, December 2014.

[39]Edelman, J., Chynoweth, B., McKiernan, G., Sweeney, C., and Schneider, S., "Instability Measurements in the Boeing/AFOSR Mach-6 Quiet Tunnel," *AIAA Paper 2016-3343*, June 2016.

[40]Babinsky, H. and Harvey, J. K., "Shock Wave-Boundary-Layer Interactions," Cambridge University Press, 2014.

[41]Brown, L. M., Boyce, R. B., Mumford, N., and O'Byrne, S., "Intrinsic Three-Dimensionality of Laminar Hypersonic Shock Wave/Boundary Layer Interactions," *AIAA Paper 2009-7205*, October 2009.

[42]Knight, D., Chazot, O., Austin, J., Badr, M. A., Candler, G., Celik, B., de rosa, D., Donelli, R., Komives, J., Lani, A., Levion, D., Nompelis, I., Panesi, Panesi, G., Pezzella, G., Reimann, B., Tumuklu, O., and Yuceil, K., "Assessment of predictive capabilities for aerodynamics heating in hypersonic flow," *Progress in Aerospace Sciences*, Vol. 90, February 2017.

[43]Oberkampf, W. L., Aeschliman, D. P., Tate, R. E., and Henfling, J. F., "Experimental Aerodynamics Research on a Hypersonic Vehicle," Sandia Report SAND92-1411, April 1993.

[44]Grey, K. A., Chynoweth, B., Edelman, J., McKiernan, G., Wason, M. P., and Schneider, S. P., "Boundary-Layer Transition Measurements in the Boeing/AFOSR Mach-6 Quiet Tunnel," *AIAA Paper 2017-0068*, January 2009.

[45]Inger, G. R., "Three-Dimensional Heat-and Mass-Transfer Effects across High-Speed Reattaching Flows," *AIAA Journal*, Vol. 15, No. 3, March 1977.

[46]de Luca, L., Cardone, G., de la Chevalerie, D. A., and Fonte, A., "Viscous Interaction Phenomena in Hypersonic Wedge Flow," *AIAA Journal*, Vol. 33, No. 12, December 1995.

[47]Ludëke, H., Radespiel, R., and Schülein, E., "Simulation of Streamwise Vortices at the Flaps of Re-entry Vehicles," *AIAA Paper 2004-0915*, January 2004.